Magnetic effects on the low-$T/|W|$ instability in differentially rotating neutron stars

Curran D. Muhlberger,[1,*] Fatemeh Hossein Nouri,[2] Matthew D. Duez,[2] Francois Foucart,[3] Lawrence E. Kidder,[1] Christian D. Ott,[4] Mark A. Scheel,[4] Béla Szilágyi,[4] and Saul A. Teukolsky[1]

[1]*Center for Radiophysics and Space Research, Cornell University, Ithaca, New York 14853, USA*
[2]*Department of Physics and Astronomy, Washington State University, Pullman, Washington 99164, USA*
[3]*Canadian Institute for Theoretical Astrophysics, University of Toronto, Toronto, Ontario M5S 3H8, Canada*
[4]*Theoretical Astrophysics 350-17, California Institute of Technology, Pasadena, California 91125, USA*

(Received 12 May 2014; published 17 November 2014)

Dynamical instabilities in protoneutron stars may produce gravitational waves whose observation could shed light on the physics of core-collapse supernovae. When born with sufficient differential rotation, these stars are susceptible to a shear instability (the "low-$T/|W|$ instability"), but such rotation can also amplify magnetic fields to strengths where they have a considerable impact on the dynamics of the stellar matter. Using a new magnetohydrodynamics module for the Spectral Einstein Code, we have simulated a differentially-rotating neutron star in full 3D to study the effects of magnetic fields on this instability. Though strong toroidal fields were predicted to suppress the low-$T/|W|$ instability, we find that they do so only in a small range of field strengths. Below 4×10^{13} G, poloidal seed fields do not wind up fast enough to have an effect before the instability saturates, while above 5×10^{14} G, magnetic instabilities can actually amplify a global quadrupole mode (this threshold may be even lower in reality, as small-scale magnetic instabilities remain difficult to resolve numerically). Thus, the prospects for observing gravitational waves from such systems are not in fact diminished over most of the magnetic parameter space. Additionally, we report that the detailed development of the low-$T/|W|$ instability, including its growth rate, depends strongly on the particular numerical methods used. The high-order methods we employ suggest that growth might be considerably slower than found in some previous simulations.

DOI: 10.1103/PhysRevD.90.104014 PACS numbers: 04.25.D-, 04.40.Dg, 04.30.Db

I. INTRODUCTION

Stellar core collapse, accretion-induced white dwarf collapse, and binary neutron star merger all naturally produce rapidly spinning neutron stars with strong differential rotation. The resulting neutron stars could be subject to well-known dynamical instabilities, and the resulting stellar deformations could produce a strong gravitational wave signal which, if detected, would provide invaluable information on these violent phenomena.

Global $m = 2$ instabilities (perturbations with an azimuthal dependence of $e^{im\phi}$) are particularly relevant for gravitational wave production. One source of such modes is the dynamical bar mode instability. However, this instability only sets in for extremely high values of the ratio of the rotational kinetic energy T to the gravitational potential energy W: $T/|W| \geq 0.27$ (with small variations depending on the equation of state and ratio of mass to radius [1–4]). Simulations have revealed another dynamical nonaxisymmetric instability that can appear at much lower $T/|W|$ if sufficient differential rotation is present [5–16]. Watts, Andersson, and Jones [17] have given compelling arguments for identifying this "low-$T/|W|$ instability", as it was called, as a form of corotation shear instability, similar in basic principle to the better-known Papaloizou-Pringle instability in thick accretion disks [18]. Namely, nonaxisymmetric modes trapped in a resonant cavity make multiple passes across a corotation radius (the radius where the mode pattern speed matches the local fluid angular speed) and are amplified on each pass. A local minimum of the radial vortensity profile has been suggested as the mechanism for mode trapping [10]. Simulations of protoneutron stars indicate that realistic core collapse scenarios can produce stars subject to this instability [19]. Indeed, the gravitational waves from this instability have been proposed as a distinctive signal from hypothesized magnetorotationally-driven galactic supernovae with rapidly rotating cores [20].

Magnetohydrodynamic simulations have shown that the dynamical bar mode instability can be suppressed by magnetic forces, although only for unrealistically high magnetic field strengths [21,22]. Fu and Lai have investigated the effect of a toroidal magnetic field on the low-$T/|W|$ instability using an analytic model, treating the star as an infinite cylinder with no vertical structure [23]. Because of the strong differential rotation, a more modest poloidal seed field ($\sim 10^{14}$ G) could wind up to a sufficiently strong toroidal field ($\sim 10^{16}$ G) within the growth

*curran@astro.cornell.edu

time of the instability (around 30 ms). The protoneutron stars most likely subject to the low-$T/|W|$ instability have strong differential rotation and potential for magnetorotational dynamo action, and in such stars magnetic fields of this magnitude are plausible [24]. Magnetic suppression could therefore eliminate the potential gravitational wave signal of core-collapse supernovae. However, Fu and Lai's model makes a number of strong simplifying assumptions: cylindrical stars, a polytropic equation of state, and purely toroidal fields. These could lead to the neglect of other important magnetohydrodynamical effects and instabilities. Thus, simulations of more realistic configurations in full 3D are needed to evaluate the robustness of the suppression mechanism.

In this work, we simulate the effects of magnetic fields on differentially-rotating neutron stars susceptible to the low-$T/|W|$ instability, and we do so using a new magnetohydrodynamics (MHD) module for the Spectral Einstein Code (SpEC)[25]. The instability is indeed suppressed for a narrow range of strong seed magnetic fields, but the more commonly observed behavior is for either magnetic fields to be too weak to affect the global quadrupole mode or for them to be sufficiently strong for magnetic instabilities to set in and actually amplify the mode. In general, we find gravitational waves comparable in magnitude to the unmagnetized case.

A. Notation

Physical equations in this work are written in geometrized units where the speed of light c and the gravitational constant G are set equal to 1. Residual dimensions can be expressed as powers of mass, for which we choose the mass of the Sun, $M_\odot$, as the unit. When discussing electromagnetic fields in the context of our simulation formalism and stability analysis, we adopt the Lorentz-Heaviside convention, absorbing a factor of $1/\sqrt{4\pi}$ into the definition of the magnetic field $\boldsymbol{B}$. However, when presenting physical results, we express all quantities in CGS-Gaussian units. In particular, $\boldsymbol{B}_{\rm LH} = \boldsymbol{B}_{\rm G}/\sqrt{4\pi}$.

We denote the Cartesian coordinates of space by x, y, z. The coordinate distance from the origin of our system is denoted by $r \equiv \sqrt{x^2+y^2+z^2}$. When cylindrical coordinates are used, $\varpi \equiv \sqrt{x^2+y^2}$ represents the coordinate distance to the z-axis, and $\phi \equiv \tan^{-1}(y/x)$ defines a point's azimuthal angle.

Tensor indices from the beginning of the Latin alphabet $(a, b, \ldots)$ represent spacetime components without reference to any particular coordinate system, while indices from the Greek alphabet $(\mu, \nu, \ldots)$ range from 0 to 3 and correspond to components in our Cartesian coordinate system of (t, x, y, z). Indices from the middle of the Latin alphabet $(i, j, \ldots)$ range from 1 to 3 and represent spatial Cartesian components. An index corresponding to a coordinate symbol $(t, \phi, \ldots)$ represents a component in an implied coordinate system (either Cartesian or cylindrical in this work).

II. NUMERICAL METHODS

To simulate the behavior of magnetized, differentially-rotating neutron stars, we solve Einstein's equations of general relativity coupled to both the relativistic Euler equations for a perfect fluid and the induction equation of ideal MHD. The solution is found using SpEC, which implements a hybrid of spectral and finite volume methods [26]. As in previous studies conducted with this code, the spacetime metric and its derivatives are evolved on a multidomain pseudospectral grid, while the hydrodynamic variables are restricted to a uniform rectilinear grid encompassing all of the matter in the system and are evolved in conservative form using a high-resolution shock-capturing finite volume scheme. This work introduces the magnetic field as a new degree of freedom and treats its evolution with an upwind constrained transport scheme on a staggered grid.

The details of our numerical treatment of this system of equations are described in Appendix A. Here we present our definitions for quantities used throughout the rest of the work:

The spacetime metric g_{ab} is decomposed into $3+1$ form with 3-metric γ_{ij}, lapse α, and shift vector β^i (see, e.g., Baumgarte and Shapiro [27]). The determinant of the 3-metric is denoted by γ. The matter in the system is modeled as a perfect fluid with rest-mass density ρ, specific internal energy ϵ, and 4-velocity u^a. An equation of state relates ρ and ϵ to the fluid's pressure P, and from these, the relativistic specific enthalpy is $h = 1 + \epsilon + P/\rho$. We denote the Lorentz factor corresponding to the fluid's velocity by $W_L \equiv \alpha u^t$.

To this we add an electromagnetic field with Faraday tensor F^{ab}, from which we define the magnetic field in a spatial slice to be $B^i = \alpha(\star F^{0i})$ (where $\star F^{\mu\nu}$ is the Hodge dual of the Faraday tensor). Several quantities of interest are naturally expressed in terms of b^a, the magnetic field in a frame comoving with the fluid:

$$b^a = (\star F^{ab}) u_b. \tag{1}$$

We adopt the assumptions of ideal MHD; namely, that the fluid is perfectly conducting.

III. SETUP

A. Physical system

Since our purpose is to study the effect of magnetic field strength and configuration on the low-$T/|W|$ instability, we focus here on one system that, in the unmagnetized case, is subject to this instability. As a starting point, we choose a differentially rotating neutron star model very similar to one of the ones studied by Corvino *et al.* [15], namely their configuration M.1.200, which they indeed find to be

unstable. Our star has a baryon mass of $M_b = 2.44\mathrm{M}_\odot$, a central density of $\rho_c = 1.16 \times 10^{-3}\mathrm{M}_\odot{}^{-2}$, and a ratio of kinetic to gravitational potential energy of $T/|W| = 0.2$ (low enough to avoid the high-$T/|W|$ dynamical bar mode instability, which becomes accessible for $T/|W| \gtrsim 0.24$ [3,28]). The degenerate component of the equation of state is given by the SLy model [29], which we implement via the fitting formula introduced by Shibata *et al.* [30]. Thermal contributions to the pressure and internal energy are included by a simple Γ-law addition to the equation of state (see Shibata *et al.*, Duez *et al.* [26]), where we have chosen $\Gamma_{\rm th} = 2$. At the start of simulations, the temperature of the star is set to zero. Thus, we ignore for the purposes of this study the significant thermal energy that would be found in a realistic protoneutron star or binary postmerger remnant scenario, but we do model the dominant cold nuclear physics component of the equation of state.

For the initial state of the star, we create an axisymmetric nonmagnetized equilibrium solution of the Einstein equations. The spacetime metric, set in quasi-isotropic coordinates, takes the form

$$ds^2 = -e^{\mu+\nu}dt^2 + e^{\mu-\nu}r^2\sin^2(\theta)(d\phi - \omega dt)^2 + e^{2\xi}(dr^2 + r^2 d\theta^2), \quad (2)$$

where μ, ν, ω, and ξ are arbitrary functions of axisymmetric space. Differential rotation is a key requirement for the instability and is incorporated by setting the initial angular velocity, $\Omega \equiv u^\phi/u^t$, according to

$$\Omega_c - \Omega = \hat{A}^{-2}u^t u_\phi = \frac{1}{\hat{A}^2 R_e^2}\left[\frac{(\Omega-\omega)r^2\sin^2(\theta)e^{-2\nu}}{1-(\Omega-\omega)^2 r^2\sin^2(\theta)e^{-2\nu}}\right], \quad (3)$$

where R_e is the coordinate equatorial radius, Ω_c is the central angular velocity, and $\hat{A}$ is a dimensionless parameter characterizing the strength of differential rotation. For the initial state of the system under study, $R_e = 7.8\mathrm{M}_\odot$, $\Omega_c = 2\pi \times 3.0$ kHz, and $\hat{A} = 1$. The ratio of polar to equatorial coordinate radii is $R_p/R_e = 0.414$. We compute the equilibrium configuration using the code of Cook, Shapiro, and Teukolsky [31].

Since the equilibrium data are axisymmetric to numerical precision, we seed the star with a small $m = 2$ perturbation in order to make the initial perturbation resolution-independent and its subsequent growth numerically convergent. This perturbation is applied to the rest-mass density and takes the form

$$\rho \to \rho\left(1 + \delta_2 \frac{x^2 - y^2}{R_e^2}\right). \quad (4)$$

The size of the initial perturbation is $\delta_2 = 2 \times 10^{-5}$. This yields an initial distortion [see Eq. (12)] of $\eta_+ = 4.08 \times 10^{-6}$. While we do not re-solve the general relativity constraint equations, the increase in the generalized harmonic constraint energy is negligible ($< 10^{-4}\%$ of its volume-averaged L^2 norm, which is 2.8×10^{-4} times that of the dynamical field gradients; see Lindblom *et al.* [32]).

TABLE I. Basic properties of the neutron star. R_e is the equatorial coordinate radius, and R_p is the polar coordinate radius. $\Delta\Omega$ is the angular frequency range—the difference between the central and equatorial rotation frequencies.

	$G, c, M_\odot = 1$	cgs
M_0	2.44	4.85×10^{33} g
$M_{\rm ADM}$	2.19	4.35×10^{33} g
R_p/R_e	0.414	0.414
ρ_c	0.00116	0.717×10^{15} g × cm^{-3}
Ω_c	0.0922	$2.98 \times 2\pi$ kHz
$\Delta\Omega$	0.0650	$2.10 \times 2\pi$ kHz

The properties of the star in its initial state are summarized in Table I. While the mass is considerably higher than would be expected for a protoneutron star (though not implausible for a binary neutron star merger remnant), we expect our conclusions regarding the interaction of magnetic fields and the low-$T/|W|$ instability to apply qualitatively to lower-mass systems. Several properties differ slightly from those of Corvino *et al.*'s MS1.200, as we did not iterate our initial data to match that model exactly. In particular, our star is roughly 2% less massive, so while we expect the overall evolution to be quite similar, we should not expect perfect correspondence in quantitative measurements.

Finally, we introduce a seed poloidal magnetic field. Following a standard practice in the numerical literature (e.g., [33–35]), we introduce a toroidal vector potential with strength

$$A_\phi = A_b \varpi^2 \max(P - P_{\rm cut}, 0)^{n_s}, \quad (5)$$

where A_b sets the overall strength of the resulting B-field, n_s controls the smoothness of the field, and the cutoff pressure $P_{\rm cut}$ (set to 4% of the central pressure) confines the initial field to regions of high-density matter. The vector potential is evaluated at cell edges, with a fourth-order curl operator producing the initial B-field at cell faces. This field is then superimposed on top of the unmagnetized equilibrium solution. While not formally self-consistent, at the field strengths we consider we expect both the deviation from equilibrium and the constraint violations in the equations of general relativity to have negligible effects on our conclusions. Specifically, the norm of the generalized harmonic constraint energy increased by $< 1\%$ with the addition of the magnetic field. Selected field lines for the initial and evolved states of the star are illustrated in Fig. 1.

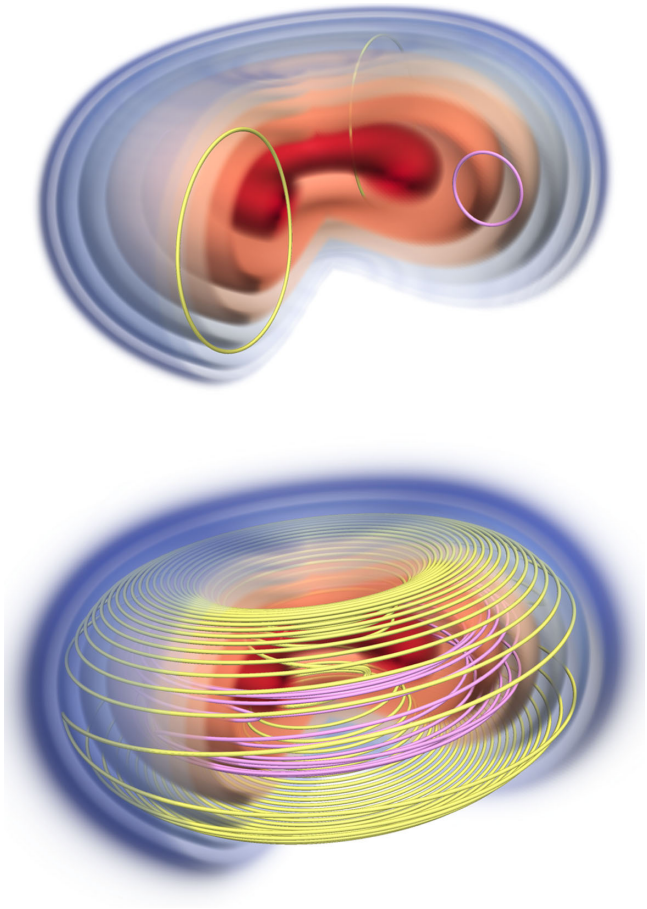

FIG. 1 (color online). Illustrations of magnetic field lines at early ($t = 0$, above) and intermediate ($t = 2160$, below) times. Contours represent regions of similar rest-mass density. Magnetic field lines are seeded at coordinate radii of $2M_\odot$ (large vertical extent; yellow) and $4M_\odot$ (small vertical extent; pink).

We explored a region of the two-parameter space $A_b \times n_s$. However, it is more intuitive to talk about magnetic field strengths measured in Gauss than the poloidal coefficient A_b. The magnetic configurations studied are summarized in Table II, which reports both the maximum strength of the B-field at $t = 0$ as well as a representative initial field strength B_0 that more closely reflects the average field in the star. We assign this representative strength to each magnetic field configuration by measuring the early growth of the magnetic energy within the star, hereafter labeled H_B [see Eq. (10)], and fitting to it the formula

$$H_B \approx B_0^2 \left(\frac{\Delta\Omega^2 R^3}{6}\right) t^2 \tag{6}$$

to solve for B_0. Here we take $\Delta\Omega = 2.1 \times 2\pi$ kHz and $R = 15.3$ km (the proper equatorial radius, as opposed to the isotropic coordinate radius reported earlier). This formula was also used by Fu and Lai in their analysis [23], easing comparisons with that work.

The dynamical importance of the magnetic field can be inferred from the ratio of the gas to magnetic pressure $\beta = 2P/b^2$ (where $b^2 \equiv b^a b_a$). For our strongest initial field, β starts no lower than 3.8×10^2.

TABLE II. Summary of the magnetic configurations studied. $B_{\max}$ is the maximum strength of the initial poloidal magnetic field, B_0 is its "representative" strength as defined in the text, and $\beta_{\min}$ is the minimum ratio of fluid pressure to magnetic pressure found initially in the interior of the star.

A_b $[G, c, M_\odot = 1]$	n_s	$B_{\max}$/G	B_0/G	$\beta_{\min}$
0	n/a	0	0	∞
0.00768	1	2.5×10^{14}	4×10^{13}	1.1×10^6
0.0379	1	1.3×10^{15}	2×10^{14}	5.2×10^4
0.0892	1	2.9×10^{15}	5×10^{14}	9.5×10^3
0.444	1	1.5×10^{16}	2×10^{15}	3.8×10^2
424	2	1.8×10^{15}	2×10^{14}	5.9×10^5
1000	2	4.1×10^{15}	5×10^{14}	1.1×10^5

B. Simulation parameters

We used several evolution grids over the course of this investigation, but our final results were achieved on a "reference" finite volume grid with $\Delta x = \Delta y = 0.17M_\odot = 250$ m and $\Delta z = 0.10M_\odot = 150$ m. Grids employed during the exploratory phase (discussed in Sec. V A) used uniform resolution and are detailed where mentioned.

Our spectral grid (for evolving the spacetime; see Fig. 2) consists of a filled sphere (using a basis of three-dimensional generalizations of Zernike polynomials; see

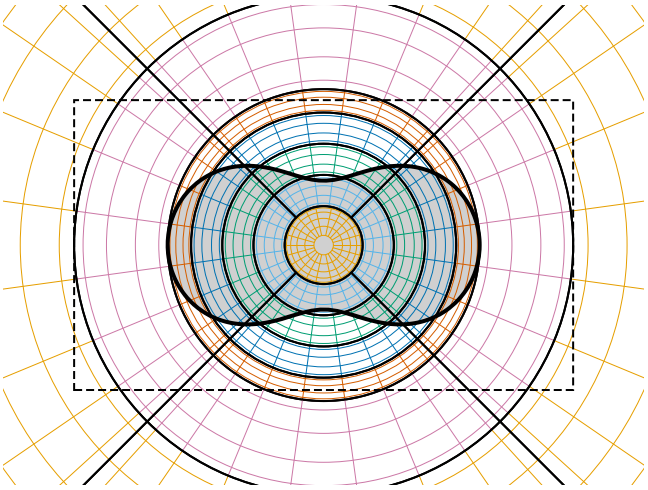

FIG. 2 (color online). Illustration of x-z slice of domain decomposition. The shaded region with a bold outline represents the initial star. The dashed rectangle represents the finite-difference domain, which has a coordinate width of $25M_\odot$ and a coordinate height of $14.5M_\odot$. For spectral subdomains, the actual reference grid has twice as many collocation points in each direction as are shown in the figure.

Appendix B) surrounded by layers of "cubed spheres"—products of Chebyshev polynomials distorted to conform to 1/6 of a spherical shell. These encompass the entire finite volume grid and are in turn surrounded by true spherical shells (a product of Chebyshev polynomials and spherical harmonics) extending to 300 stellar equatorial radii. The spectral resolution of our reference grid corresponds to spherical harmonics out to $l = 21$ for the central sphere and $l = 17$ for the outer spheres. The radial dimensions of these spheres are resolved by 12 and 11 collocation points, respectively. The cubed spheres contain 12 radial points and 20 transverse points.

IV. ANALYSIS

To study the low-$T/|W|$ instability in our simulations and the effects that magnetic fields have on it, we consider several global measures of the simulation results as functions of time. These include various energy integrals, defined as follows:

Rest mass:

$$M_b = \int \rho W_L \sqrt{\gamma} d^3x. \tag{7}$$

Kinetic energy:

$$T = \frac{1}{2}\int \rho h W_L u_i v^i \sqrt{\gamma} d^3x, \tag{8}$$

where $v^i \equiv u^i/u^0$.

Internal energy:

$$U = \int \rho W_L \epsilon \sqrt{\gamma} d^3x. \tag{9}$$

Magnetic energy:

$$H_B = \frac{1}{2}\int b^2 W_L \sqrt{\gamma} d^3x. \tag{10}$$

Since total energy is conserved (and our hydrodynamic evolution is conservative), we can infer the change in gravitational energy from the sum of the changes in these nonvacuum energies. Some of this is lost in the form of gravitational waves, which emit $2.1 \times 10^{-4}\mathrm{M}_\odot$ of energy over the duration of the simulation in the unmagnetized case. Any remaining difference must therefore be a change in the gravitational binding energy of the star.

Following previous studies, we consider the quadrupole moment of the rest mass density about the origin (which is the initial center-of-mass):

$$I^{ij} = \int \rho W_L x^i x^j \sqrt{\gamma} d^3x. \tag{11}$$

To reduce this to a scalar measure, we consider two polarizations of the x and y components of the quadrupole tensor,

$$\eta_+(t) \equiv \frac{I^{xx}(t) - I^{yy}(t)}{I^{xx}(0) + I^{yy}(0)} \tag{12}$$

$$\eta_\times(t) \equiv \frac{2I^{xy}(t)}{I^{xx}(0) + I^{yy}(0)}, \tag{13}$$

and, following Corvino *et al.* [15], take their magnitude to define the "distortion parameter" η:

$$|\eta(t)| = \sqrt{\eta_+^2(t) + \eta_\times^2(t)}. \tag{14}$$

Note that the numerical atmosphere surrounding the star (see Sec. A 2 c) has the potential to bias integral measurements like those above. A common solution is to impose density or radius thresholds when summing the integrand. However, because our fluid grid only covers the region immediately around the star and does not extend into the wave zone, the effect of the atmosphere on these measurements is negligible.

The invariant strength of the magnetic field is simply the magnitude of b^a, whose square is equal to

$$b^2 = \frac{B^2}{W_L^2} + \left[B^i\left(\frac{u^j}{W_L} + \frac{\beta^j}{\alpha}\right)\gamma_{ij}\right]^2. \tag{15}$$

To report physical results, we convert this strength to CGS-Gaussian units via

$$|B_{\mathrm{CGS}}| = \frac{\sqrt{4\pi b^2}}{1\mathrm{M}_\odot}\left(\frac{c^2}{GM_\odot}\right)\left(\frac{c}{\sqrt{4\pi\epsilon_0 G}}\right) \times 10^4\ \mathrm{G}$$
$$= \sqrt{b^2} \times 8.352 \times 10^{19}\ \mathrm{G}. \tag{16}$$

We also consider the evolution of some quantities in a Lagrangian frame of reference. To do this, we seed "tracer" particles in the fluid and evolve their positions according to the fluid velocity in our Eulerian evolution frame. The resulting trajectories provide useful information in their own right, and observing quantities along those trajectories allows for their Lagrangian analysis.

Finally, in order to accurately monitor the growth of instabilities of arbitrary m in a robust manner, we consider an additional measure of nonaxisymmetry that differs from diagnostics used in previous investigations. Our approach is discussed below.

A. Azimuthal modes

Previous studies have analyzed the "Fourier power" of m-modes of a field ψ by integrating the quantity $\psi e^{im\phi}$. Some have performed this integral over a ring, capturing

the power at a single radius and height within the system [10,19]. Others, including Corvino *et al.*, have performed a volume integral. While the latter approach incorporates contributions from the entire system, it has several disadvantages. The integrand is in general discontinuous at the origin for $m > 0$, and thus naive numerical computations of $|P_m|$ can produce spurious results (for example, computing a finite volume integral with a gridpoint at the origin will result in nonzero $m > 0$ power for axisymmetric data). Additionally, m-modes of ψ whose phase changes with radius or height will be biased (for instance, a tightly wound spiral structure will produce canceling contributions to the integral for each infinitesimal annulus). Diagnostics defined in terms of multipole moments, like η, do not suffer the discontinuity problem, but radial cancellations still cause, for instance, the quadrupole moment to be a potentially poor representation for what one would intuitively call "$m = 2$ power."

A hybrid approach is to sum the power of ψ in several rings, thus sampling the field at multiple heights and radii. More generally, ψ can be multiplied by a set of orthogonal window functions isolating particular subsets of the domain, with volume integrals used to compute the power of each product. These functions would approach the origin as ϖ^m, ensuring smoothness there, and would be localized at various radii, avoiding cancellation from spiral structure. A natural choice for such a set of functions are the radial and vertical cardinal functions associated with a basis for functions over a cylinder (for example, the product of Zernike polynomials over a disk with Legendre polynomials in z). These functions are smooth, orthogonal, and generally localized around their corresponding node.

In fact, this approach is equivalent to a spectral measure of m-power, defined in Eq. (C9), where the Fourier components of ψ are decomposed into a set of basis functions, and the squared magnitude of the spectral coefficients are summed (see Appendix C for proof). It is this definition of m-power, which we denote with $P_m[\psi]$, that we employ in our analysis. To account for possible center-of-mass motion, the origin is chosen to follow the measured center-of-mass $(\int \boldsymbol{x}\rho W_L\sqrt{\gamma}d^3\boldsymbol{x}/\int \rho W_L\sqrt{\gamma}d^3\boldsymbol{x})$ of the system.

V. RESULTS

Having established the accuracy and convergence of our code on standard test problems (see Appendix A 3), we can now compare our findings regarding the unmagnetized low-$T/|W|$ instability with previous simulations of the same system, confirming the baseline against which magnetized results will be compared.

A. Unmagnetized instability

When simulating the unmagnetized system, we find the behavior of the low-$T/|W|$ instability to depend sensitively on the reconstruction algorithm employed by the code (see Appendix A 2 for the role and implementation of reconstruction in our evolution scheme). In particular, the growth of the distortion parameter $|\eta|$ was not convergent with resolution for the majority of reconstructors considered (a more thorough investigation is the subject of ongoing work). We are, however, able to obtain consistent results using WENO5 reconstruction, as shown in Fig. 3.

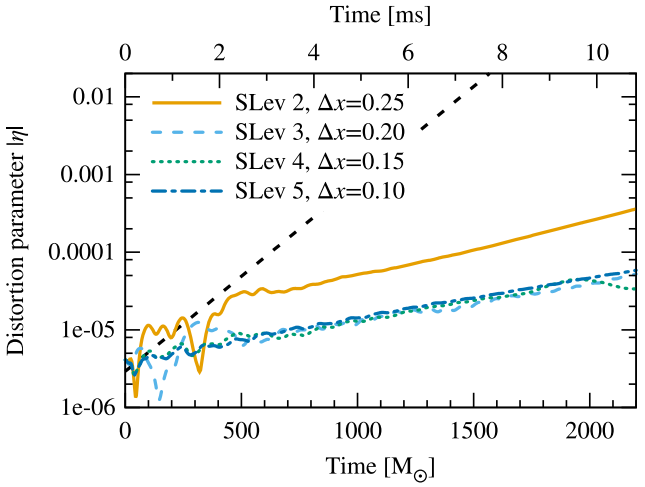

FIG. 3 (color online). Consistency of the growth rate of the low-$T/|W|$ instability when using WENO5 reconstruction at various resolutions (no magnetic field is present). The black dashed line represents the approximate growth rate found by Corvino *et al.* for M.1.200. Results from resolutions of $\Delta x \lesssim 0.2\mathrm{M}_\odot$, while not formally convergent, are in good agreement and are clearly distinct from those of Corvino *et al.* "SLev" indicates the spectral resolution level, with higher levels corresponding to finer resolution (the "reference" grid uses SLev 4), and grid spacings are measured in solar masses.

Even when using WENO5 reconstruction, insufficient resolution, particularly in the vertical direction, can introduce spurious features in the distortion parameter's evolution at intermediate times and otherwise increase the simulation's sensitivity to other choices in numerical methods. We see long-term consistency in the growth of η when $\Delta z \lesssim 0.1\mathrm{M}_\odot$.

We follow the unmagnetized system through the saturation and initial decay of the instability, as shown in Fig. 4. The growth is exponential with a time constant of $\tau \approx 3.6$ ms, and the amplitude of the instability saturates when the distortion parameter reaches $|\eta|_{\max} \approx 0.035$. This is the reference against which our magnetized results will be measured.

Comparing to the results of Corvino *et al.* [15] (who used the piecewise parabolic method for reconstruction), we find a large disagreement in the overall growth rate of η. Our simulations exhibited clean exponential growth of one mode for over 30 ms with a characteristic time of $\tau \approx 3.6$ ms. For comparison, from Fig. 3 in Corvino *et al.*'s work we estimate an overall growth time of $\tau \approx 0.88$ ms.

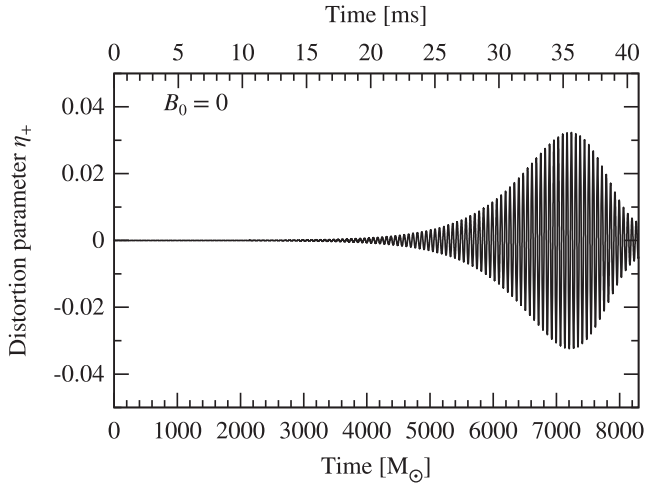

FIG. 4. Growth and saturation of the unmagnetized low-$T/|W|$ instability as expressed in the "plus" polarization of the distortion parameter η. The "cross" polarization exhibits the same behavior with a phase shift. Compare to Corvino *et al.* Fig. 3.

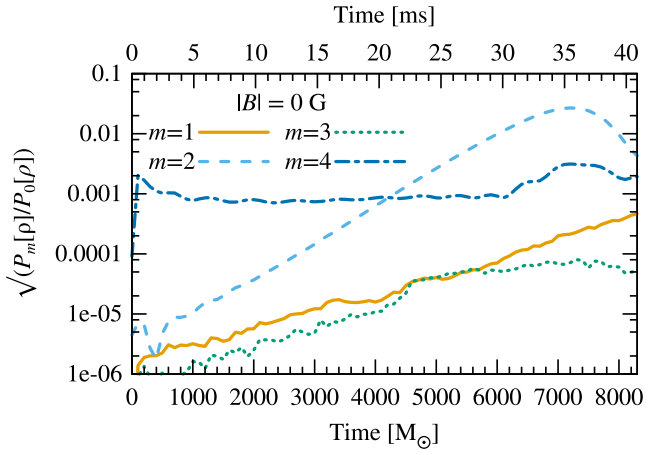

FIG. 5 (color online). Relative power of ρ in azimuthal modes for $m = 1$–4. Note that measurements of $m = 4$ power have a noise floor of 10^{-3} due to the Cartesian nature of the grid.

This rate is illustrated by the dashed line in Fig. 3 and results in saturation of the instability considerably sooner than in our simulations. Saturation amplitudes, however, agree to within a factor of two (0.035 vs 0.055). In fact, the simulation in that paper found growth of several modes, some at rates more similar to ours, while their fastest-growing mode does not exactly match ours. Apparently, the numerical (especially reconstruction) algorithm can have a significant effect on the spectrum of unstable modes accessible to and excited by the star, whether by seeding them or by damping them. We hope to clarify such influences in future work.

Overall, the growth profile we observe for η is much more similar to those Corvino *et al.* report for stars with even lower values of $T/|W|$ (0.15 and 0.16), showing smooth exponential growth followed by decay, than what they report for $T/|W| = 0.2$.

The relative power of the density perturbation in the lowest few Fourier modes is shown in Fig. 5. Unlike Ott *et al.* [19], but consistent with Scheidegger *et al.* [14] and Corvino *et al.*, we find $m = 2$ to be the dominant mode. This is also the mode whose interaction with magnetic fields was analyzed in detail by Fu and Lai [23]. Note that, because the low $T/|W|$ generally triggers growth at many azimuthal modes, which one becomes dominant will depend both on the exact profile of the star and on the structure of the initial perturbation, so there is not necessarily any incompatibility between the Ott *et al.* results and other simulations.

B. Magnetic effects

We find that the presence of a magnetic field could have two competing effects on the growth of the $m = 2$ fluid instability. Simulations with fields of 4×10^{13} G and greater demonstrate suppression of the instability, with the distortion parameter saturating at a significantly smaller value (3–50×lower) than in an unmagnetized star. Even stronger fields (starting at 5×10^{14} G), however, made the star susceptible to a small-scale (few gridpoints per wavelength) magnetic instability that rapidly amplified the $m = 2$ distortion of the star (in addition to other modes). This instability may operate at lower field strengths as well, but there its effects would not be resolvable at our current resolution. The net behavior for all simulated cases is plotted in Figs. 6 and 7 and is qualitatively independent of the seed field geometry (parametrized by n_s; in particular, the threshold for instability appears to be the same).

Simulations of these magnetically unstable cases were halted prior to the original saturation time, as

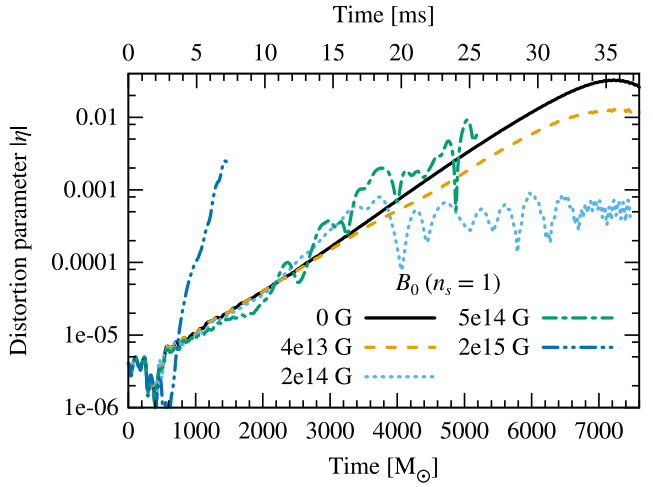

FIG. 6 (color online). Range of behavior of distortion parameter η at different magnetic field strengths for $n_s = 1$. Curves that terminate at early times developed significant outflows, making further evolution impractical on our grid.

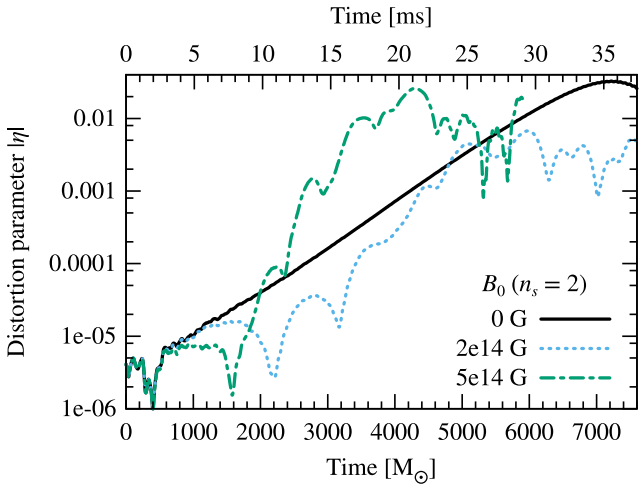

FIG. 7 (color online). Range of behavior of distortion parameter η at different magnetic field strengths for $n_s = 2$, showing same classes of behavior as when $n_s = 1$ (see Fig. 6).

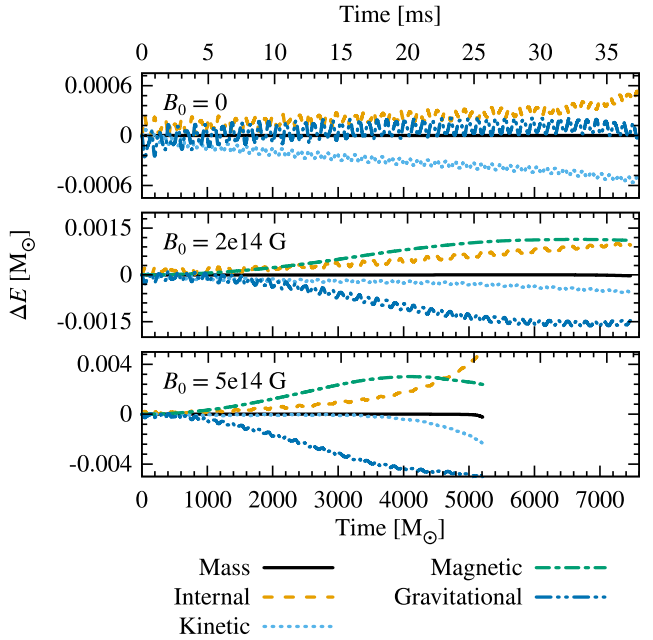

FIG. 8 (color online). Energy exchange for three magnetic field strengths ($n_s = 1$ for each case). The change in gravitational energy is inferred from the sum of the changes in the other energies.

magnetized outflows of matter began to leave the grid. Both magnetically-dominated and pressure-dominated matter leave the star relatively isotropically with mildly relativistic velocities ($W_L \lesssim 0.15$). The stronger the magnetic field, the sooner these outflows develop. Similar outflows have been noted in previous investigations [36,37], though due to the small size of our grid, we cannot make quantitative comparisons.

1. Suppression of the low-$T/|W|$ instability

When we observe suppression, we would like to determine whether the mechanism is consistent with that proposed by Fu and Lai. Unfortunately, the correspondence is far from clear. In particular, while magnetic winding produces peak toroidal field strengths comparable to those considered in their work (and surpassing their threshold for suppression of 2×10^{16} G), the total magnetic energy saturates at much lower values than they deem necessary for suppression to take place. This reflects the fact that the toroidal field distribution in our simulations differ from the linear function of cylindrical radius assumed by Fu and Lai. Our runs with initial poloidal field strengths on the order of $B_0 \approx 2 \times 10^{14}$ G wind up toroidal fields as strong as 10^{17} G but with magnetic energies of only half a percent of the star's kinetic energy. For comparison, their model implies that such fields would possess magnetic energy equivalent to 20% of T, which they find is the minimum energy ratio for suppression to occur. We expect that the field strength in the region of the corotation radius is the more relevant measure of the field's effect, so we believe the field strength observed in our simulations are adequate to probe the suppression mechanism.

We see that magnetic winding increases the magnetic energy in the star at the expense of gravitational potential energy, as shown in Fig. 8, but saturates within 30 ms in the cases we considered (prior to the saturation of the low-$T/|W|$ instability). Matter near the core of the star is compacted, increasing the central density. The internal energy of the matter also increases in magnetized scenarios, but the kinetic energy is barely affected in most cases. For the magnetically-unstable systems, however, kinetic energy from nonazimuthal fluid velocities grows exponentially at late times as the rotational kinetic energy begins to decrease at an amplified rate (the separation of rotational and nonrotational kinetic energy is not shown in the figure). This likely corresponds to small-scale fluid oscillations associated with the magnetic turbulence described below.

Other comparisons are difficult as well. In Fig. 5 of their paper, Fu and Lai show that the Lagrangian displacement of fluid elements should diverge at the corotation radius during the low-$T/|W|$ instability, but that this resonance should split in the presence of a strong toroidal magnetic field. Using tracers, we do see an amplification in radial displacement in the vicinity of the corotation radius in the unmagnetized case (see Fig. 9), but the response is so broad that we cannot resolve any splitting when magnetic fields are added.

Nevertheless, there are clues pointing to a resonance splitting. In particular, spectrograms of the distortion parameter show a split peak when magnetic suppression is observed (see Fig. 10). The magnitude of splitting for $B_0 = 2 \times 10^{14}$ G, $n_s = 2$ is about $\Delta\omega \approx 2\pi \times 0.1$ kHz. Defining the angular Alfvén speed,

$$\omega_A \equiv B^{\phi}/(\varpi\sqrt{\rho}), \tag{17}$$

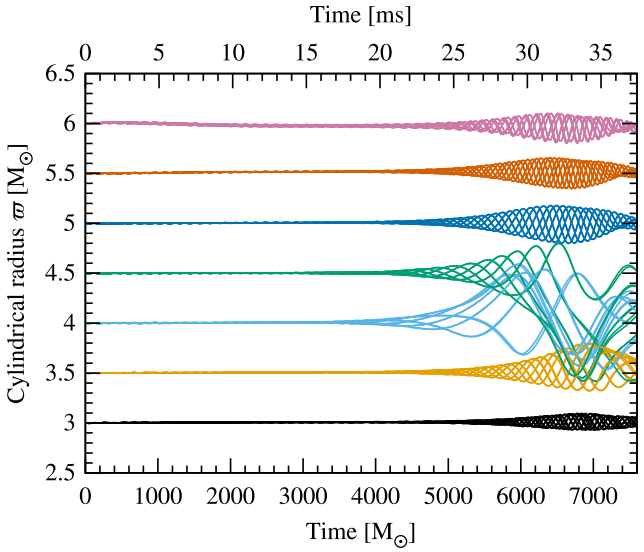

FIG. 9 (color online). Lagrangian displacement of tracer particles seeded at various cylindrical radii for an unmagnetized star. For each initial radius, 12 tracers were distributed uniformly in azimuth. The corotation radius for this system is at $\varpi \approx 4.25 M_\odot$.

and the slow magnetosonic wave frequency,

$$\omega_s \equiv \sqrt{\frac{c_s^2}{c_s^2 + (B^\phi)^2/\rho}} m\omega_A, \tag{18}$$

(where c_s is the adiabatic sound speed), resonances are expected at $\Delta\omega = \omega_s$ and (in the full 3D case) $\Delta\omega = m\omega_A$. In the strongly magnetized regions of the star, the observed splitting agrees with the values of ω_s and $2\omega_A$ to within a factor of four. Given the differences in the particular systems under study, this is reasonably consistent with Fu and Lai's proposed mechanism.

2. Magnetic instability

When the initial magnetic field exceeds $B_0 = 5 \times 10^{14}$ G, our simulations start to exhibit strong magnetic instability. This instability results both in the amplification of low-m global modes in the star and in turbulence at the smallest scales we can resolve on our grid. The marginally-resolved nature of this instability complicates its identification and interpretation.

The growth of small-scale features is most visible in poloidal field components, as illustrated in Figs. 11 and 12, while large-scale nonaxisymmetric structure is easily seen in the much stronger toroidal field (see Fig. 13). The crest-to-crest separation of the poloidal perturbations is measured to be approximately $\lambda \sim 1 M_\odot$, which is resolved by roughly five gridpoints. This suggests that the unstable modes are only marginally resolved, so we cannot expect their subsequent evolution to be more than qualitatively correct (at best).

In fact, magnetically-driven instabilities in the fluid are not unexpected. Magnetic winding generates a strong toroidal field in the interior of the star, and toroidal field gradients are potentially unstable to kink (Tayler) and buoyancy (Parker) instabilities [38–42]. For a toroidal field centered on the rotation axis, the Tayler instability can occur at cylindrical radii ϖ less than the radial pressure scale height H_P (defined as in [40,43] as $2c_s^2/g_\varpi$, with g_ϖ denoting the radial acceleration) for positive $dB^\phi/d\varpi$.

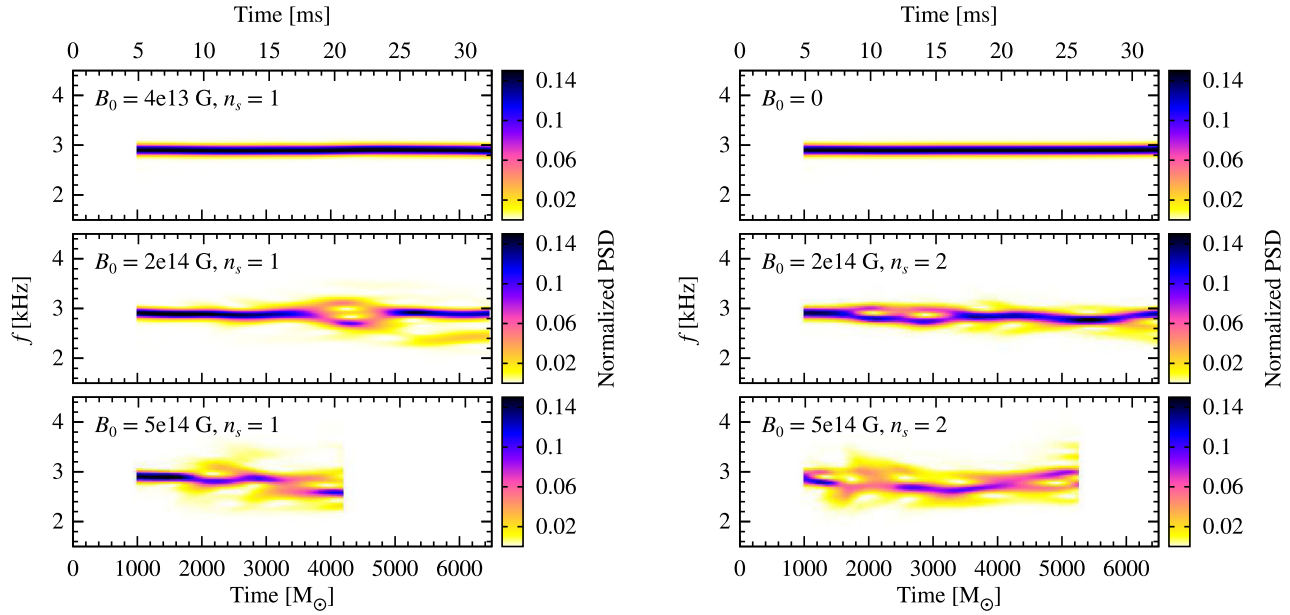

FIG. 10 (color online). Spectrograms of the quadrupole moment I_{xy} for six cases. Power spectral density (PSD) estimated via FFT periodogram using Welch's method with a Hann window.

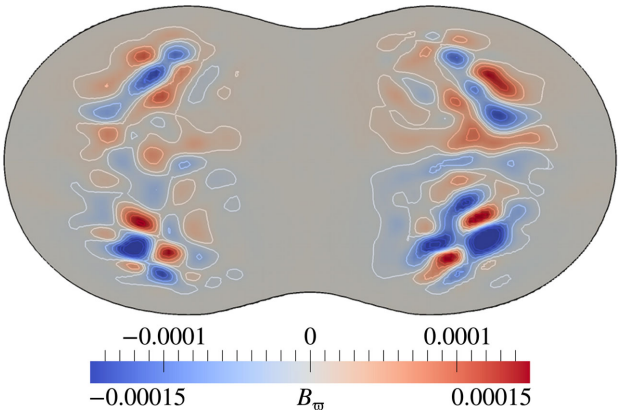

FIG. 11 (color online). Magnitude of radial component of B-field in the y-z plane at $t = 3760\mathrm{M}_\odot$ for $B_0 = 5 \times 10^{14}$ G, $n_s = 2$.

Kink instabilities have in fact recently been identified in 3D magnetized core-collapse simulations [37]. The Parker instability can be triggered by radial or vertical field gradients (negative $dB^\phi/d\varpi$ for $\varpi > H_P$ or negative dB^ϕ/dz). The growth rate of the Tayler instability is of order the angular Alfvén speed ω_A for weak rotation and ω_A^2/Ω for strong rotation, where $\Omega \gg \omega_A$ is the condition for strong rotation [44]. Growth time scales for the Parker instability are similar. Although much analytic work on field-gradient instabilities assumes weak differential rotation, the Parker instability has been found to be operable

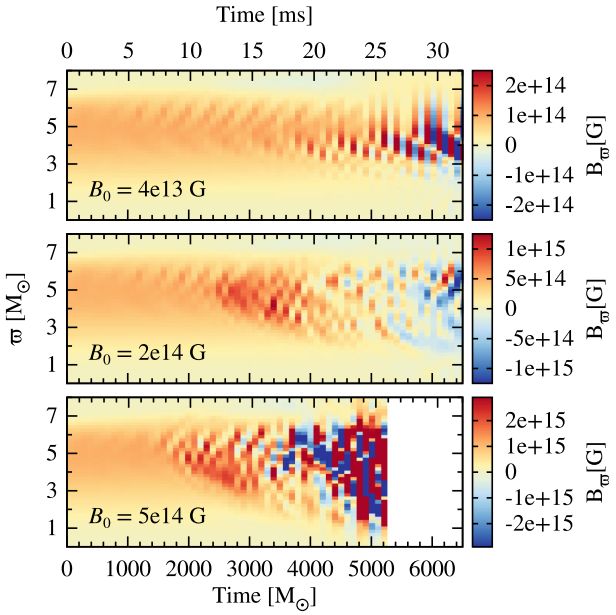

FIG. 12 (color online). Magnitude of radial component of B-field vs radius vs time in the $z = 1$ plane for three configurations ($n_s = 1$ in all cases), illustrating the onset of turbulence. Color bars are scaled relative to the initial B-field strength. Plot inspired by the analysis of Franci *et al.* [22].

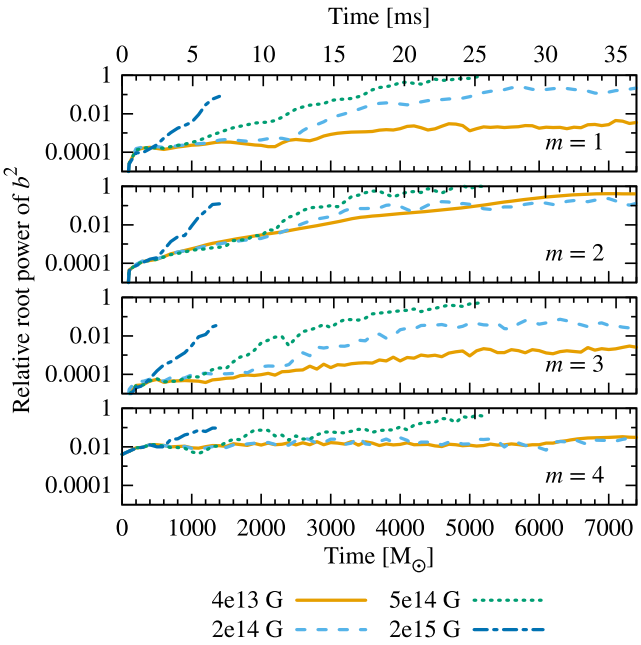

FIG. 13 (color online). Power of b^2 in azimuthal modes for $m = 1$–4. Except in the most strongly magnetized systems, the $m = 4$ power does not rise above that of the ambient grid mode. The growing strength of the magnetic field is factored out by normalizing by the $m = 0$ power; thus, trends shown here represent growth of the proportional power of nonaxisymmetric modes.

even in some flows with strong shear [45]. In our magnetically-unstable cases, ω_A/Ω is $\mathcal{O}(1/2)$ at the corotation radius, suggesting an intermediate regime between weak and strong rotation.

In addition to the above-mentioned field gradient-driven instabilities, differential rotation will also trigger shear-driven instabilities. The most famous is the classic magnetorotational instability (MRI), an axisymmetric instability triggered by a nonzero (but arbitrarily small) poloidal field and an outward-decreasing rotation rate [46]. More generally, the MRI can also be found in nonaxisymmetric configurations [47,48], in which case the background toroidal field can also contribute to seeding the instability [40,47]. The fastest-growing unstable mode grows on a time scale of $\sim\Omega^{-1}$ and has a wave number given by

$$\Omega/\sqrt{-g_{00}} \sim \boldsymbol{k}\cdot\boldsymbol{v}_A \approx \frac{k^\varpi B^\varpi + k^z B^z + mB^\phi/\varpi}{\sqrt{\rho h + b^2}} \qquad (19)$$

(on the relativistic factor, see Siegel *et al.* [49]). The main challenge for numerical MHD simulations is to resolve the MRI wavelength $\lambda_{\mathrm{MRI}} = 2\pi|\boldsymbol{k}|^{-1}$. Since the field is usually azimuthally-dominated, we see that $m \neq 0$ modes are potentially easier to resolve, a fact also recently noted by Franci *et al.* [22], who resolve MRI-like field growth only in nonaxisymmetrically-unstable stars. On the other hand, the growth of a given nonaxisymmetric mode will be expected to

terminate when the mode becomes too tightly wound [47]. In fact, it has long been known that even a purely toroidal field can seed a shear instability [40,47,48], although the growth time scales tend to be longer than those associated with poloidal seed fields, except for the case of very high m, and in that case even a small poloidal field would be expected to radically alter the flow [48].

Given the presence of differential rotation and a poloidal magnetic field, our system is certainly susceptible to the MRI; what is less clear is our ability to resolve it. Siegel *et al.* [49] state that a minimum of five gridpoints per wavelength was required to resolve the MRI in their simulations. Using Eq. (19), we can estimate what the wavelength of the fastest-growing unstable mode would be at any point in our simulation, optimizing over propagation directions. Comparing this to our effective grid resolution in those directions, we find that when turbulence starts to develop in our systems, there are $\mathcal{O}(\text{few})$ gridpoints per wavelength in the unstable regions of the star even for $m = 0$ modes, and when considering higher m, these unstable regions begin to meet the criterion of five gridpoints per wavelength. Therefore, resolving the MRI, if only marginally, is conceivable given our resolution and magnetic field strengths.

One approach to diagnosing the source of turbulence is to measure the growth rates of observed instabilities and match them to linear predictions. As mentioned above, the Tayler and Parker instabilities should grow at a rate between ω_A and ω_A^2/Ω, while the MRI's growth rate is Ω, independent of the B-field magnitude. The rotational frequency of the star in the region of magnetic instability (which occurs in the vicinity of the corotation radius) is about $\Omega \approx 1.45 \times 2\pi$ kHz.

Looking at the growth of the most magnetized point on the grid (see Fig. 14) reveals exponential behavior at rates that increase with the magnetic field strength. This scaling, in addition to the magnitude of the rates, is incompatible with the MRI [while the expected rate of Ω is an approximation derived from accretion disks, the numerical prefactor for our system is expected to be $\mathcal{O}(3/4)$, insufficient to explain the discrepancy].

Considering the field gradient-driven instabilities, the "weak rotation" rate of ω_A is too large as well and also does not match the observed scaling with B-field strength. The "strong rotation" prediction, however, while still larger than observed, is only off by a factor of a few and is the closest match to the data in terms of scaling. This suggests that, while the MRI is potentially resolvable with our techniques, the observed local maximum B-field growth is most attributable to field gradient instabilities. Shear instabilities are almost certainly still present and impacting the dynamics, however, and likely play a large role in less-magnetized cases where we currently cannot resolve them. In fact, their expected growth rates suggest that they would dominate the dynamics on relevant timescales were they resolved.

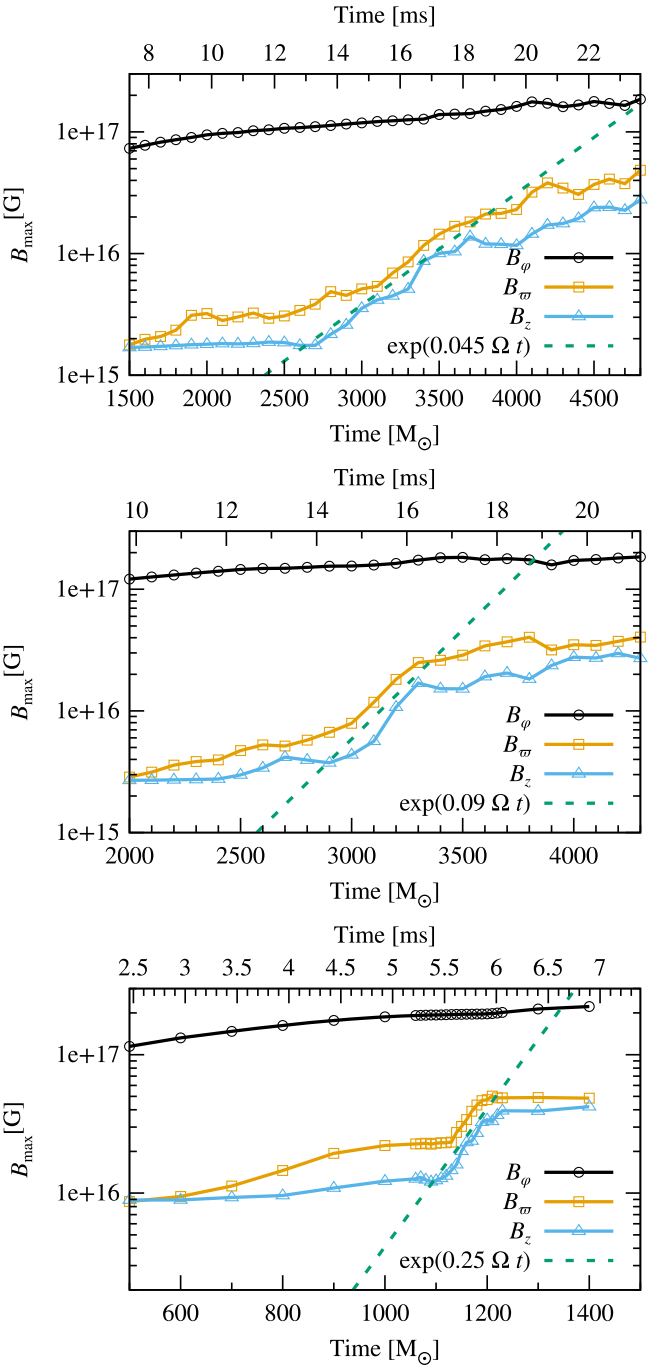

FIG. 14 (color online). Growth of the maximum of the cylindrical components of the B-field for three cases: $B_0 = 5 \times 10^{14}$ G, $n_s = 1$ (top), $B_0 = 5 \times 10^{14}$ G, $n_s = 2$ (middle), and $B_0 = 2 \times 10^{15}$ G, $n_s = 1$ (bottom). The temporal resolution during the period of rapid growth for the last case is $10\times$ finer than our default.

C. Detectability

To help put these results in an astrophysical context, we consider the detectability of gravitational waves produced by the (unmagnetized) low-$T/|W|$ instability for this system. We follow the procedure outlined by Sutton

[50]. Given both polarizations of the gravitational wave strain, h_+ and $h_\times$, at some distance from the source, define the root-sum-square amplitude $h_{\rm rss}$ to be

$$h_{\rm rss} = \sqrt{\int (h_+^2(t) + h_\times^2(t))dt}. \tag{20}$$

For a narrow-band signal from a rotating system like ours, we expect the emitted gravitational wave energy $E_{\rm GW}$ to be well-approximated by

$$E_{\rm GW} \approx \frac{2}{5}\frac{\pi^2 c^3}{G} f_0^2 r^2 h_{\rm rss}^2, \tag{21}$$

where f_0 is the central frequency of the signal. The effective detection range $\mathcal{R}_{\rm eff}$ for a narrow-band burst signal is given by

$$\mathcal{R}_{\rm eff} = \beta\sqrt{\frac{G}{\pi^2 c^3}\frac{E_{\rm GW}}{S(f_0) f_0^2 \rho_{\rm det}^2}}, \tag{22}$$

where $S(f)$ is the one-sided noise power spectrum for the target detector, $\rho_{\rm det}$ is the threshold signal-to-noise ratio for detection, and β is a geometrical factor related to the polarization of the waves. Specializing to rotating sources, this becomes

$$\mathcal{R}_{\rm eff} = 0.698\frac{r h_{\rm rss}}{\rho_{\rm det}}\sqrt{\frac{2}{5}\frac{1}{S(f_0)}}. \tag{23}$$

We extract gravitational waves from our simulations at a radius of $400\mathrm{M}_\odot$ using Regge-Wheeler-Zerilli techniques [51] and consider the strains h_+ and $h_\times$ for an observer above the axis of rotation. For the unmagnetized star considered in this work, the gravitational wave frequency is sharply peaked at 2.9 kHz (this is slightly lower than the 3.2 kHz primary peak observed by Corvino *et al.* [15]). If we consider only the instability's initial growth through saturation, the total emitted gravitational wave energy is 3.68×10^{50} erg ($2.06 \times 10^{-4}\mathrm{M}_\odot$). Using the ZERO_DET_HIGH_P noise curve for Advanced LIGO [52] and a signal-to-noise threshold of $\rho_{\rm det} = 20$, this instability would be detectable out to 92 kpc.

The emitted gravitational wave energy is significantly larger than what was found in core-collapse supernovae simulations [13,14] ($E_{\rm GW} \sim 10^{46}$–10^{47} erg for a similar simulation length). However, the difference can easily be understood by noting that the neutron star considered in this work rotates significantly more rapidly (with the wave signal peaking at 2.9 kHz vs ~0.9 kHz in the core-collapse results) and is also more massive than protoneutron stars are expected to be. Since $E_{\rm GW} \propto M^2\Omega^6$, this accounts for most of the difference in the emitted gravitational wave energy. On the other hand, the more slowly rotating neutron stars emit waves at a more favorable frequency, improving their detectability.

The effect of magnetic fields on detectability is difficult to discern from our data, as outflows prevented us from evolving the most highly magnetized systems long enough to see the instability saturate. For $B_0 = 5 \times 10^{14}$ G, $n_s = 2$, the distortion parameter peaks nearly as high as the saturation value in the unmagnetized case while the frequency spectrum at that time peaks at a slightly lower (and more favorable) value, suggesting that a gravitational wave signal from magnetic instabilities could be just as detectable as that of the unmagnetized low-$T/|W|$ instability. On the other hand, mildly magnetized cases exhibit a suppressed distortion parameter with an unchanged frequency spectrum. Using the quadrupole approximation, and the fact that $\mathcal{R}_{\rm eff}$ is linear in $h_{\rm rss}$, this means that the effective detection range is decreased by factor of ~2.4 for $B_0 = 4 \times 10^{13}$ G, $n_s = 1$, and by a factor of ~34 for $B_0 = 2 \times 10^{14}$ G, $n_s = 1$, for an observer above the axis of rotation.

VI. CONCLUSIONS

In writing a MHD module for SpEC, we have expanded the range and fidelity of astrophysical systems that can be simulated while still taking advantage of its highly accurate spacetime evolution. The future scope of this code includes many systems of contemporary interest, including magnetized compact binary coalescence, but here we focus our attention on instabilities in differentially rotating neutron stars.

Of significant relevance to existing literature regarding these stars is the variability in simulated growth rates when using different resolutions and reconstruction methods. We find qualitative convergence when using high resolution and high-order reconstruction, but these results differ significantly from those of lower-accuracy techniques and of some previous studies. Further investigation of such instabilities' delicate dependence on simulation methods is warranted.

Regarding the low-$T/|W|$ instability, it is clear that poloidal magnetic fields on the order of 10^{14} G can have a strong effect on the distribution of mass in differentially rotating neutron stars and therefore on their gravitational wave signatures. However, while suppression of the instability is feasible, it occurs in a small region of parameter space. B-fields strong enough to enable the suppression mechanism are likely also strong enough to trigger magnetic instabilities, accelerating the growth of a mass quadrupole moment rather than suppressing it.

In our simulations, with clean poloidal initial fields, the window between the onsets of magnetic suppression and magnetic instability—roughly 4×10^{13} G–5×10^{14} G—is rather small, and future runs with increased resolution may lower the upper bound still further. Therefore, amplification of matter perturbations seems to be the more likely

magnetic effect, with peak amplitudes comparable to those in the unmagnetized case. The spectrum of the gravitational waves, while perhaps possessing more structure, will also remain peaked near the same frequency. As a result, even with such extreme field strengths, the net effect on burst detectability is likely minor.

Regarding Fu and Lai's conclusions, we find some disagreement between their predictions for cylindrical stars and our simulations of realistic ones. In particular, they concluded that suppression would occur once the magnetic energy H_B reached about 20% of the kinetic energy T. However, the magnetic energy in our simulations peaks at 0.56% of T, yet we still find suppression in some cases. Despite this, we agree on the minimum strength of the poloidal seed field, roughly 10^{14} G. Additionally, the frequency spectrum of the instability is consistent with their proposed mechanism for suppression.

Uncertainties in our investigation include the details of the formation of the star and its seed field, as Nature will not be nearly as clean as the system we considered. Additionally, we expect that if the MRI were fully resolved, it would grow on such a short time scale that it would dominate the effects observed here.

Future work to understand the details of the suppression mechanism could investigate the effects of purely toroidal fields, removing the complications of magnetic winding and the MRI. On the other hand, the impact of the magnetic instabilities could be better understood by increasing resolution and by extending the simulations to observe their saturation behavior. Additionally, the systematic effects of reconstruction order and grid resolution on the growth rate of this particular instability warrant further investigation. Lastly, while this paper has limited itself to studying the growth of instabilities, the later evolution of such stars, after the commencement of magnetically-driven driven winds, would be a very astrophysically interesting subject for future numerical modeling.

ACKNOWLEDGMENTS

We extend our thanks to D. Lai for inspiring this investigation, to M. Boyle for advice on several occasions, and to F. Hébert for catching errors in the text. We also extend our gratitude to S. Bernuzzi, R. De Pietri, B. Giacomazzo, and L. Rezzolla, whose correspondence after the first version of this paper helped to clarify the comparison between their simulations and ours. The authors at Cornell gratefully acknowledge support from National Science Foundation (NSF) Grants No. PHY-1306125 and No. AST-1333129, while the authors at Caltech acknowledge support from NSF Grants No. PHY-1440083 and No. AST-1333520 and NSF CAREER Award No. PHY-1151197. Authors at both Caltech and Cornell also thank the Sherman Fairchild Foundation for their support. F. Foucart gratefully acknowledges support from the Vincent and Beatrice Tremaine Postdoctoral Fellowship, from the NSERC of Canada, from the Canada Research Chairs Program, and from the Canadian Institute for Theoretical Astrophysics. Finally, the authors at WSU acknowledge support through NASA Grant No. NNX11AC37G and NSF Grant No. PHY-1402916. Some computations were performed on the GPC supercomputer at the SciNet HPC Consortium [53], funded by the Canada Foundation for Innovation under the auspices of Compute Canada, the Government of Ontario, Ontario Research Fund–Research Excellence, and the University of Toronto. This work also used the Extreme Science and Engineering Discovery Environment (XSEDE) through allocations No. TG-PHY100033 and No. PHY990002, supported by NSF Grant No. OCI-1053575. Additionally, this research was performed in part using the Zwicky computer system operated by the Caltech Center for Advanced Computing Research and funded by NSF MRI No. PHY-0960291 and the Sherman Fairchild Foundation.

APPENDIX A: NUMERICAL METHODS

1. Metric evolution

As in previous studies using SpEC, the spacetime is evolved according to Einstein's equations in generalized harmonic form [32], and the coordinates x^a are assumed to obey

$$g_{ab}\nabla^c\nabla_c x^b = H_a \tag{A1}$$

for some gauge source function H_a (where ∇_a is the covariant derivative operator associated with g_{ab}). To reduce the equations to first-order form, we evolve the derivatives of the spacetime metric g_{ab}, defined as

$$\Phi_{iab} \equiv \partial_i g_{ab} \tag{A2}$$

$$\Pi_{ab} \equiv -n^c\partial_c g_{ab}, \tag{A3}$$

where n^a is the normal to a spacelike slice. This slicing defines a $3+1$ decomposition of the metric into a 3-metric γ_{ij}, lapse α, and shift vector β^i (see, e.g., Baumgarte and Shapiro [27]), with line element given by:

$$ds^2 = -\alpha^2 dt^2 + \gamma_{ij}(dx^i + \beta^i dt)(dx^j + \beta^j dt). \tag{A4}$$

The spacetime variables g_{ab}, Φ_{iab}, and Π_{ab} are evolved according to the principal parts and constraint damping terms in Appendix A of Foucart *et al.* [54] (augmented with the matter and magnetic source terms described below), and the gauge source H_a is evolved according to the "frozen" condition in that work. The damping parameters for the system considered in this work are distributed according to:

$$\gamma_0(r) = \frac{0.1}{M_{\rm NS}} f(r) + \frac{0.1}{M_{\rm NS}}, \tag{A5}$$

$$\gamma_1(r) = -1, \tag{A6}$$

$$\gamma_2(r) = \frac{1.5}{M_{\rm NS}} f(r) + \frac{0.1}{M_{\rm NS}}, \tag{A7}$$

where $f(r)$ is given by:

$$f(r) = e^{-r/(6M_{\rm NS})} \tag{A8}$$

and $M_{\rm NS}$ is the ADM mass of the neutron star.

The presence of matter and magnetic fields results in a nonzero stress-energy tensor T_{ab}, and this shows up in additional source terms when evolving the spacetime fields. In particular, the vacuum evolution equation for Π_{ab} is modified as follows:

$$\partial_t \Pi_{ab} = \cdots - 2\alpha\left(T_{ab} - \frac{1}{2} g_{ab} T^{cd} g_{cd}\right). \tag{A9}$$

The stress-energy tensor for our treatment of MHD is given in Eq. (A10). Note that we expect the magnetic contributions to T_{ab} to be small, even for our strongest field strengths (magnetic pressure is at most 1% of fluid pressure at $t = 0$).

2. Magnetohydrodynamics

The stress-energy tensor of a magnetized perfect fluid, as described in Sec. II, is given by

$$T_{ab} = \rho h u_a u_b + P g_{ab} + F_{ac} F_b{}^c - \frac{1}{4} F^{cd} F_{cd} g_{ab}. \tag{A10}$$

Additionally, we adopt the assumption of ideal MHD that the fluid is perfectly conducting:

$$F^{ab} u_b = 0 \tag{A11}$$

(that is, the electric field vanishes in a frame comoving with the fluid). This eliminates the electric field as an independent quantity and leaves eight degrees of freedom: five for the fluid and three for the magnetic field.

The state of the fluid at each gridpoint is represented in the code by the "primitive variables" ρ, T, u_i, and B^i, where T (not to be confused with kinetic energy) is a variable, related to the temperature, parametrizing the thermal pressure. The precise relationship of T to the temperature and thermal pressure is allowed to vary with the equation of state. Given ρ and T, the equation of state specifies the pressure $P(\rho, T)$ and specific internal energy $\epsilon(\rho, T)$.

In order to express the equations of their evolution in conservative form, we recompose them into the following set of "conservative" variables:

$$\rho_* = \sqrt{\gamma} W_L \rho \tag{A12}$$

$$\tilde{\tau} = \sqrt{\gamma}\left(W_L \rho (W_L h - 1) - P + B^2 - \frac{1}{2}\frac{B^2 + (B^i u_i)^2}{W_L^2}\right) \tag{A13}$$

$$\tilde{S}_i = \sqrt{\gamma}\left(W_L \rho h u_i + \frac{1}{W_L}(B^2 u_i - B^j u_j B^k \gamma_{ik})\right) \tag{A14}$$

$$\mathcal{B}^i = \sqrt{\gamma} B^i \tag{A15}$$

(see also, e.g., [27,55]). Here, γ is the determinant of the 3-metric, $W_L \equiv \alpha u^t$ is the Lorentz factor corresponding to the fluid's velocity, and $B^2 \equiv B^i B^j \gamma_{ij}$. These "conservative" evolved variables map to the set of "primitive" variables through an inversion procedure described in Secs. A 2 a and A 2 b.

The conservative variables are evolved according to:

$$\partial_t \rho_* + \partial_i(\rho_* v^j) = 0, \tag{A16}$$

$$\partial_t \tilde{\tau} + \partial_i(\alpha^2 \sqrt{\gamma} T_{0i} - \rho_* v^i) = -\alpha \sqrt{\gamma} T^{\mu\nu} \nabla_\nu n_\mu, \tag{A17}$$

$$\partial_t \tilde{S}_i + \partial_i(\alpha \sqrt{\gamma} T^j{}_i) = \frac{1}{2} \alpha \sqrt{\gamma} T^{\mu\nu} \partial_i g_{\mu\nu}, \tag{A18}$$

where $v^i = u^i / u^t$ is the "transport velocity" of the fluid.

To compute the behavior of the magnetic field, we define an analog to the electric field,

$$\mathcal{E}_i \equiv -[ijk] v^j \mathcal{B}^k, \tag{A19}$$

and then evolve the magnetic field according to

$$\partial_t \mathcal{B}^i = -[ijk] \partial_j \mathcal{E}_k, \tag{A20}$$

where $[ijk]$ is $+1$ for an even permutation of the indices and -1 for an odd permutation. This evolution is constrained by the zero-monopole criterion,

$$\nabla^{(3)} \cdot \boldsymbol{B} = \partial_i \mathcal{B}^i = 0 \tag{A21}$$

(where $\nabla^{(3)}$ is the covariant derivative operator corresponding to the 3-metric). In general, a numerical evolution scheme for the magnetic field will not preserve this constraint, so we adopt a constrained transport framework (first used by Yee [56] and later for generally relativistic MHD by Evans and Hawley [57]) to do so.

Our constrained transport implementation follows the prescription for "upwind constrained transport" proposed by Londrillo and Del Zanna [58] and described in detail by Del Zanna *et al.* as implemented in the ECHO code [59]. In particular, the longitudinal components of $\mathcal{B}^i$ are evolved at cell faces. This presents a convenient definition of magnetic divergence at cell centers as the second-order divided

difference of $\mathcal{B}^i$. The constrained transport algorithm guarantees that the time derivative of this quantity will be zero to machine precision. When the B-field itself is needed at cell centers, fourth-order polynomial interpolation is used, since discontinuities in the longitudinal direction are forbidden. Such interpolation is also used when metric quantities are needed at cell faces, as these fields are expected to be smooth.

In order to compute the fluxes of the evolution variables, nonsmooth matter quantities must be reconstructed at cell faces and edges. Our code allows a choice of reconstructors, including a second-order monotonized centered (MC2) limiter [60] and a fifth-order weighted essentially nonoscillatory (WENO5) scheme [61–63]. The HLL approximate Riemann solver [64] determines a single value for the flux on each interface. Flux derivatives are computed as second-order divided differences, making our scheme formally second-order accurate (that is, we do not perform the DER operation employed by the ECHO code). However, higher-order reconstructors, while not affecting the convergence rate, can greatly improve the accuracy of the code (see Sec. V A) at the expense of parallelization efficiency (their larger stencils require additional ghost zones).

In common with other high-resolution shock-capturing codes, SpEC requires procedures for inverting the relationship between primitive and conservative variables, along with a prescription for maintaining a tenuous atmosphere around the star. The addition of a magnetic field necessitates changes to these algorithms, the details of which we describe below.

a. Full MHD primitive variable recovery

We mostly follow the prescription of Noble *et al.* [65] for recovering primitive variables from the evolved conservative variables, that is the task of numerically inverting equations (A12)–(A15). We define

$$\tilde{S}^2 = \gamma^{ij}\tilde{S}_i\tilde{S}_j, \tag{A22}$$

$$H = h(\rho, T)\rho W_L^2, \tag{A23}$$

so that the relations between primitive and conservative variables can be written as

$$\tilde{S}^2 W_L^2 = \gamma(W_L^2 - 1)(B^2 + H)^2 - W_L^2\frac{(\tilde{S}_i B^i)^2(B^2 + 2H)}{H^2}, \tag{A24}$$

$$-\frac{\rho_* W_L^2 + \tilde{\tau} W_L^2}{\sqrt{\gamma}} = \frac{B^2}{2} + W_L^2\left(\frac{(\tilde{S}_i B^i)^2}{2\gamma H^2} - B^2 - H + P(\rho, T)\right). \tag{A25}$$

We solve these equations for (T, W_L^2) using the GNEWTON method as implemented by the GNU Scientific Library [66], subject to the constraint $W_L^2 \geq 1$. These equations are more challenging for the root-finding algorithm than the $B = 0$ case, especially in cases where the magnetic and/or kinetic energy of the fluid is large compared to its rest mass energy. When the 2D root-finder for (T, W_L^2) fails, we switch to a simple 1D bracketing algorithm solving for H (W_L is then considered as a known function of H).

b. Low density force-free primitive variable recovery

Recovery of the full set of primitive variables can be difficult or impossible at low-density, magnetically-dominated gridpoints. Fortunately, it is also unnecessary. Our treatment of such points is similar to that in Ref. [67]. For each gridpoint, the code first attempts to solve the full 2D system for (T, W_L^2). If a root cannot be found, it checks that the failing gridpoint is in the force-free regime by checking the following conditions:

(1) $\rho W_L/B^2 < 0.001$;
(2) $B^2 > \sqrt{\tilde{S}^2/\gamma}$, which is necessary to have $B^2 > \mathcal{E}^2$;
(3) $(\tilde{S}_j B^j)^2/(B^2\rho_*^2) < 10$ to prevent very large velocities along field lines.

If the point satisfies these conditions, then the code attempts a simpler 1D primitive variable recovery that ignores the internal energy of the gas.

First, we solve for the 4-velocity:

$$u_i = \frac{W_L}{B^2}\left(-\frac{\epsilon_{ijk}(\epsilon^{jlm}\tilde{S}_l B_m)B^k}{\sqrt{\gamma}B^2 + \rho_* h W_L} + \frac{(\tilde{S}_j B^j)B_i}{W_L\rho_* h}\right). \tag{A26}$$

Assuming $T = 0$, $h = 1$, and using the normalization condition $W_L^2 = 1 + \gamma^{ij}u_i u_j$, we find

$$W_L^2 = 1 + \frac{W_L^2}{B^4}\left(\frac{\epsilon_{ijk}(\epsilon^{jlm}\tilde{S}_l B_m)B^k}{\sqrt{\gamma}B^2 + \rho_* W_L}\right)^2 + \frac{(\tilde{S}_j B^j)^2}{B^2\rho_*^2}. \tag{A27}$$

The velocity $\boldsymbol{u}$ is composed of a parallel (to the magnetic field) part and a perpendicular part $W_L^2 = 1 + u_\parallel^2 + u_\perp^2$, so we have

$$u_\perp^2 = \frac{W_L^2}{B^4}\left(\frac{\epsilon_{ijk}(\epsilon^{jlm}\tilde{S}_l B_m)B^k}{\sqrt{\gamma}B^2 + \rho_* W_L}\right)^2, \tag{A28}$$

$$u_\parallel^2 = \frac{(\tilde{S}_j B^j)^2}{B^2\rho_*^2}. \tag{A29}$$

Equation (A27) is solved for W_L^2 with a 1D Newton-Raphson root solver; the other variables can be inferred from the solved W_L and the assumed $T = 0$. For force-free points with very low densities, or force-free points where we fail to solve Eq. (A27), we remove the density-dependent terms in Eq. (A27) and set u_i to the drift velocity $(u_\perp)_i$. We note that the $h = 1$ approximation used

above would have to be adjusted when using a nuclear equation of state in which $h(\rho \to 0, T \to 0)$ is slightly less than one (i.e. when the binding energy of nucleons is taken into account, and the specific internal energy of the fluid is negative when $\rho \to 0$).

c. Atmosphere treatment

The methods used for the evolution of relativistic fluids often assume that $\rho > 0$. In order to avoid numerical problems in regions where no fluid is present, we have to impose $\rho \geq \rho_{\rm floor}$ everywhere. In this simulation, $\rho_{\rm floor}$ is set to 10^{-14} and $\rho_{\rm floor}/\rho_{\rm max}$ is about 8×10^{-12}. However, numerical errors in the evolution of low-density fluid can easily lead to values of conservative variables for which the inversion problem has no solution. We thus need appropriate prescriptions to:

(i) Modify the conservative variables, if necessary, to force them to correspond to some set of primitive variables;
(ii) Require the primitive variables (mainly T and u_a) in the low-density region to be physically reasonable.

For a given ρ_* and B^i, limits to the allowable range of $\tilde{\tau}$ and $\tilde{S}_i$ come from considering the limit of zero internal energy ($P = 0$, $h = 1$). In this limit, we can write $\tilde{S}^2$ as a function of W_L^2:

$$\tilde{S}^2 = \frac{\rho_*^2 (W_L + \frac{\sqrt{\gamma} B^2}{\rho_*})^2 (W_L^2 - 1)}{W_L^2 + 2\frac{\sqrt{\gamma}}{\rho_*} B^2 \mu^2 W_L + \frac{\gamma}{\rho_*^2} B^4 \mu^2}, \tag{A30}$$

where $\mu \equiv B^i \tilde{S}_i / \sqrt{B^2 \tilde{S}^2}$. W_L is given by a fifth-order polynomial equation

$$0 = W_L^3 + \left(\frac{\sqrt{\gamma} B^2}{\rho_*} - \frac{\tilde{\tau}}{\rho_*} - 1 \right) W_L^2 - \frac{\sqrt{\gamma} B^2}{2\rho_*} \left(1 + \frac{\mu^2 (W_L + \frac{\sqrt{\gamma} B^2}{\rho_*})^2 (W_L^2 - 1)}{W_L^2 + 2\frac{\sqrt{\gamma}}{\rho_*} B^2 \mu^2 W_L + \frac{\gamma}{\rho_*^2} B^4 \mu^2} \right). \tag{A31}$$

This equation has a real solution $W_L \geq 1$ if and only if the condition $B^2 \leq 2\tilde{\tau}/\sqrt{\gamma}$ is satisfied. Thus, we can "fix" our conservative variables ($\tilde{\tau}$ and $\tilde{S}_i$) by imposing:

$$\tilde{S}_i \leq \sqrt{\frac{\tilde{S}^2_{\rm max}}{(\tilde{S}^0)^2}} \tilde{S}^0_i, \tag{A32}$$

$$\tilde{\tau} \geq \frac{\sqrt{\gamma} B^2}{2}, \tag{A33}$$

where $\tilde{S}^2_{\rm max}$ is the solution to Eqs. (A30) and (A31), and $\tilde{S}^0$ is the value of $\tilde{S}$ before it is "fixed." This recipe to fix conservative variables is similar to what is introduced by Etienne *et al.* [67], except that they fix $\tilde{\tau}$ and $\tilde{S}$ using stricter "sufficient conditions" for invertibility [Eqs. (A48)–(A50) in their work] for points deep inside their black hole horizon, while for points elsewhere they only fix $\tilde{\tau}$ using Eq. (A32).

d. Additional adjustments to the low-density evolution

We also impose several restrictions on the low-density fluid in order to avoid extreme heating and relativistic speeds in the atmosphere. This must be done differently in magnetospheric regions than in nonmagnetic regions, because in the former, the fluid velocity encodes information about the electric field that should not be sacrificed.

For regions with low B^2/ρ, we choose a threshold density $\rho_{\rm atm} > \rho_{\rm floor}$, and require that for $\rho < \rho_{\rm atm}$ we have $T = 0$ and $u_i = 0$. Additionally, in order to avoid a sharp transition from the "live" evolution to the atmosphere prescription, we add a smoothing region for $\rho_{\rm atm} < \rho < 10\rho_{\rm atm}$ where we require $h - 1 \leq \kappa(h_{\rm max} - 1)$ and $u^2 \leq \kappa u^2_{\rm max}$, with $\kappa = (\rho - \rho_{\rm atm})/(9\rho_{\rm atm})$. $h_{\rm max}$ and $u^2_{\rm max}$ are values larger than the enthalpies and velocities encountered in the high-density region of the simulation.

On the other hand, for magnetically dominated low-density regions, we have the same treatment as in weakly magnetic regions for h and for $u_{i\|}$ [the component of the 4-velocity along field lines, cf. Eq. (A29)], i.e. $u^2_\| \leq \kappa u^2_{\rm max}$ for $\rho_{\rm atm} < \rho < 10\rho_{\rm atm}$, and $u_{i\|} = 0$ for $\rho < \rho_{\rm atm}$. The perpendicular (drift) part of velocity [Eq. (A28)] can contain, even for very low densities, physically meaningful information about the electric field, so it is controlled much more weakly, by imposing the limit $u^2_{\perp\,\rm max} \leq u^2_{\rm max}$ for $\rho < 10\rho_{\rm atm}$.

Finally, a half-stencil's worth of points are frozen at atmosphere levels along all outer boundaries. This "boundary condition" avoids the complexities of one-sided differencing and has no effect on the bulk evolution of the matter provided that the grid is large enough (for the system considered here, magnetic fields are initially confined to high-density regions, and we halt the simulation upon the detection of significant outflows).

3. Test problems

The spacetime and hydrodynamics components of SpEC have been tested previously [26,68]. Here, we check the performance of our new MHD module, using a similar test suite as Duez *et al.* [69]. In particular, we study its accuracy and convergence by comparing results to known analytical solutions exhibiting a range of nontrivial behaviors, including shocks and strong gravity.

a. One-dimensional relativistic tests

To test the shock-capturing methods used in SpEC, we evolve a set of one-dimensional problems first proposed by Komissarov [70]. The initial data consist of two homogeneous states separated by a discontinuity at $x = 0$. The initial conditions for each test are listed in Table III. We

TABLE III. Initial data for the shock tests

Test	Initial state for $x < 0$	Initial state for $x > 0$
Fast shock	$\rho = 1,\ P = 1$	$\rho = 25.48,\ P = 367.5$
($t_{\rm final} = 2.5$)	$u_i = (25, 0, 0),\ B^i = (20, 25.02, 0)$	$u_i = (1.091, 0.3923, 0),\ B^i = (20, 49, 0)$
Slow shock	$\rho = 1,\ P = 10$	$\rho = 3.323,\ P = 55.36$
($t_{\rm final} = 2.0$)	$u_i = (1.53, 0, 0),\ B^i = (10, 18.28, 0)$	$u_i = (0.9571, -0.6822, 0),\ B^i = (10, 14.49, 0)$
Switch-off	$\rho = 0.1,\ P = 1$	$\rho = 0.562,\ P = 10$
($t_{\rm final} = 1.0$)	$u_i = (-2, 0, 0),\ B^i = (2, 0, 0)$	$u_i = (-0.212, -0.590, 0),\ B^i = (2, 4.71, 0)$
Switch-on	$\rho = 0.00178,\ P = 0.1$	$\rho = 0.01,\ P = 1$
($t_{\rm final} = 2.0$)	$u_i = (-0.765, -1.386, 0),\ B^i = (1, 1.022, 0)$	$u_i = (0, 0, 0),\ B^i = (1, 0, 0)$
Shock tube 1	$\rho = 1,\ P = 1000$	$\rho = 0.1,\ P = 1$
($t_{\rm final} = 1.0$)	$u_i = (0, 0, 0),\ B^i = (1, 0, 0)$	$u_i = (0, 0, 0),\ B^i = (1, 0, 0)$
Shock tube 2	$\rho = 1,\ P = 30$	$\rho = 0.1,\ P = 1$
($t_{\rm final} = 1.0$)	$u_i = (0, 0, 0),\ B^i = (0, 20, 0)$	$u_i = (0, 0, 0),\ B^i = (0, 0, 0)$
Collision	$\rho = 1,\ P = 1$	$\rho = 1,\ P = 1$
($t_{\rm final} = 1.22$)	$u_i = (5, 0, 0),\ B^i = (10, 10, 0)$	$u_i = (-5, 0, 0),\ B^i = (10, -10, 0)$
Wave	$\rho = 1,\ P = 1$	$\rho = 1,\ P = 1$
($t_{\rm final} = 2.5$)	$u_i = -0.4133 \cdot (0, \cos x, \sin x),\ B^i = (1, \cos x, \sin x)$	$u_i = -0.4133 \cdot (0, \cos x, \sin x),\ B^i = (1, \cos x, \sin x)$

integrate the relativistic MHD equations from $t = 0$ to $t = t_{\rm final}$ (also given in Table III). The fluid follows a Γ-law equation of state with $\Gamma = 4/3$:

$$P = \rho^{4/3} + \rho T, \tag{A34}$$

$$\epsilon = 3\frac{P}{\rho}, \tag{A35}$$

where we have now defined the code's internal temperature variable T for the Γ-law case such that ρT is the thermal pressure of the fluid. To facilitate comparisons with previously published results, we use the same resolution as in Duez *et al.* [69], where the same tests were performed (see Figs. 7–8 and Table II of that work): our numerical domain covers the region $x = [-2, 2]$, and uses 400 grid points (higher resolution results are also provided to test the convergence of our code). The tests are performed with both the MC2 reconstructor used by Duez *et al.* and the WENO5 reconstructor that we prefer in most of our simulations. We use fourth-order Runge-Kutta time stepping, with a Courant factor of 0.5 ($dt = 0.005$), except for the *fast shock* problem using WENO5 reconstruction, for which we use a Courant factor of 0.25 (the evolution is unstable for a Courant factor of 0.5, an issue which was also noted by Duez *et al.* when using the third-order piecewise parabolic method for reconstruction).

Fast and slow shocks: For these two tests, the shock front satisfies the relativistic Rankine-Hugoniot jump conditions [71]. The exact solution to the evolution of the fluid equation is known, with the shock propagating at constant speed while the fluid variables on each side of the shock remain constant [70,72]. The *fast shock* test is the hardest test for our code: it evolves a strong shock, with the shock front moving relatively slowly on the grid ($0.2c$) but the fluid being highly relativistic (Lorentz factor $W_L = 25.02$). As already noted, it is the only test that is unstable when using a Courant factor of 0.5 (for WENO5 reconstruction). It is also fairly sensitive to the choice of variables that are interpolated from cell centers to cell faces when computing the fluxes entering the conservative hydrodynamics equations: if we interpolate the transport velocity v^i, the shock evolves as expected, while if we interpolate the spatial components of the 4-velocity u_i the shock immediately stalls. Considering that in practice, in 3-dimensional evolutions of neutron stars or binary mergers, we do not reliably evolve fluid elements with $W_L \sim 25$ (the occurrence of such high Lorentz factors is prevented by the corrections applied to the velocity and temperature of low-density points in the atmosphere), this difference is unimportant in practice. The *fast shock* test is mostly evolved in order to verify that our implementation of the MHD equations is correct in the limit of ultrarelativistic fluids. In fact, because of the practical advantages of using u_i instead of v^i, we usually reconstruct the former ($W_L = \sqrt{1 + g^{ij}u_i u_j}$ is always well defined while $W_L = 1/\sqrt{1 - g_{ij}v^i v^j}$ is not if numerical errors in the low-density regions cause v^i to satisfy $g_{ij}v^i v^j > 1$). In Figs. 15 and 16, we show the result of that test when using the MC2 reconstruction method (and reconstructing v^i), for 400 and 4000 grid points. The results converge toward the solution at the expected first-order rate. The *slow shock* test is generally less extreme. As in previous studies [69,70,73], we observe that the evolution is very accurate on the left side of the shock, while oscillations are visible on the right side of the shock (see Fig. 15). Although these oscillations converge away as we increase the resolution, they do so more slowly than expected past 200-400 points in the evolution domain (convergence order of ~0.6). This is the only test for which we do not observe at least first-order convergence.

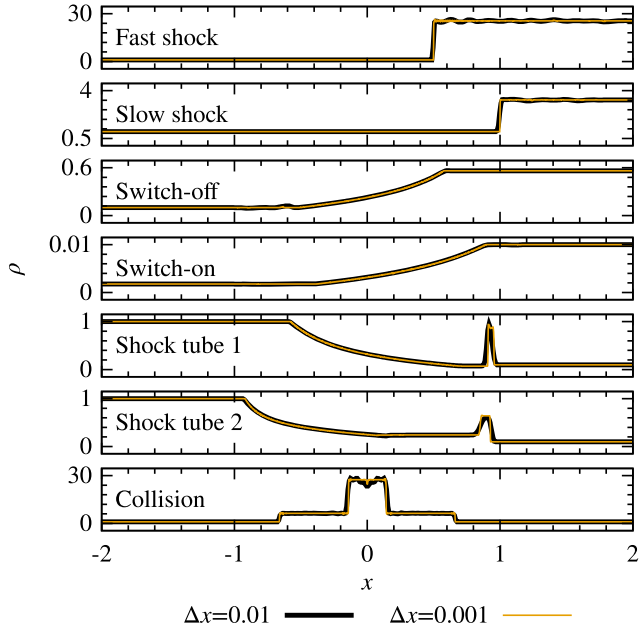

FIG. 15 (color online). Rest-mass density at $t = t_{\rm final}$ for the shock tests described in Table III, shown for two resolutions ($N = 400$ and $N = 4000$ points).

Other shock tests: The five other one-dimensional shock tests, for which results are presented in Figs. 15 and 16, are comparable to previously published results in accuracy (for the simulations using 400 points), and convergent when the resolution is increased to 4000 points. As expected, the convergence is fairly slow (first-order), which explains why sharp features remain visible even at high resolution. These tests cover a wide range of potential behaviors (shock waves, rarefaction waves, contact discontinuities), and indicate that the shock capturing methods implemented in SpEC are capable of handling the discontinuities which are likely to arise in our simulations.

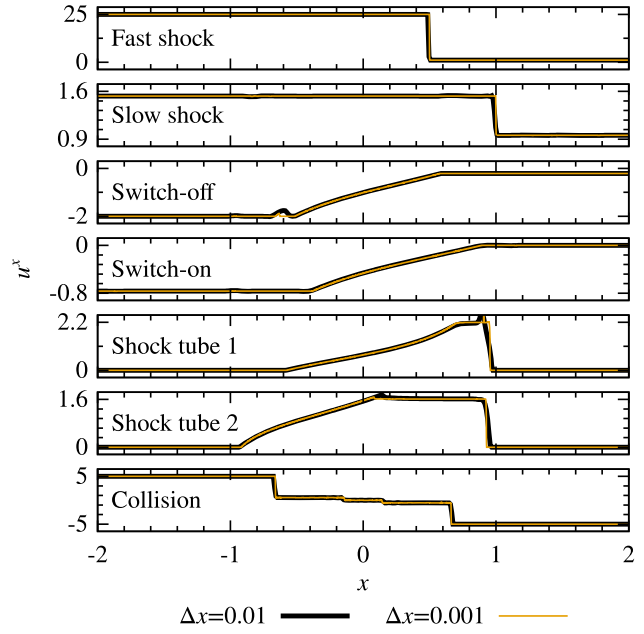

FIG. 16 (color online). Velocity at $t = t_{\rm final}$ for the shock tests described in Table III, shown for two resolutions ($N = 400$ and $N = 4000$ points).

Wave: The last one-dimensional test to which we submit our code is the propagation of a wave on a periodic grid. In this case, all variables are continuous, and the error in the simulations should be second-order convergent. In the exact solution, the initial profile (given in Table III) simply propagates with velocity $v = 0.3820$. The error in the density ρ at the end of the simulation for 3 different resolutions (50, 100, and 200 points per wavelength) is shown in Fig. 17, rescaled for the assumed second-order convergence. Our results also appear in good agreement with the theoretical predictions for this smooth configuration.

b. Bondi accretion

We also test the ability of our code to evolve a magnetized fluid in the strong gravitational field of a black hole. We check its ability to maintain stationary and spherically symmetric accretion onto a Schwarzschild black hole according to the relativistic Bondi accretion solution. This test is nontrivial since we have an extremely strong gravitational field and relativistic fluid which contains nonzero magnetic terms. There is also an exact solution to which we can compare our numerical results.

We write the metric in the Kerr-Schild coordinates; as a result, all the variables are well-behaved at the horizon (horizon penetrating). We fix the metric for this test and evolve the fluid equations only.

For this test, we evolve the same configuration used by Duez *et al.* [69]. The accretion rate is $\dot{M} = 1$, the sonic radius is at $r = 8M$ (where M is the mass of the black hole), and the equation of state obeys a $\Gamma = 4/3$ power law [see

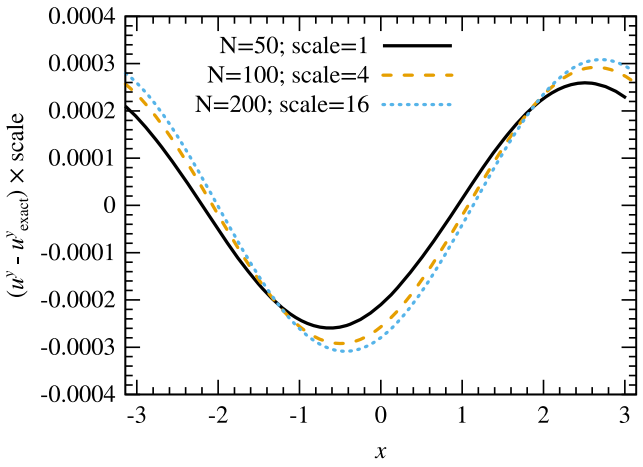

FIG. 17 (color online). Error in the final value of u^y for the *wave* test at 3 resolutions ($N = 50$, $N = 100$, $N = 200$), rescaled for the expected second-order convergence.

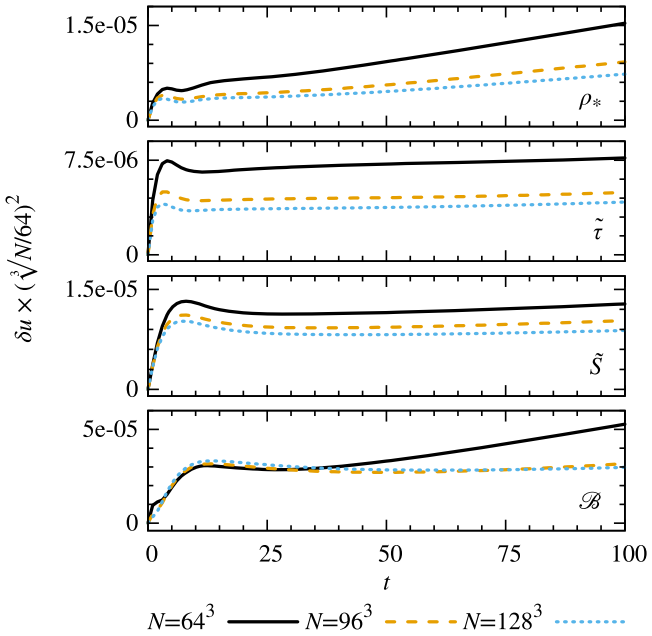

FIG. 18 (color online). Error norm for the Bondi test at three resolutions, rescaled for second-order convergence.

Eqs. (A34)–(A35)]. We freeze the hydro evolution variables at the inner and outer boundaries. We set the inner boundary radius outside of the horizon at $r = 2.8M$ (the horizon is at $r = 2M$), and the outer boundary is placed at $r = 9M$; the Cartesian grid extends $\pm 10M$ along each axis.

We evolve this accretion flow at three different resolutions: 64^3, 96^3, and 128^3. The initial magnetic field is radial such that $b^2/\rho = 1$ and the solution is stationary. Reconstruction is performed using WENO5. We add Kreiss-Oliger dissipation [74] to the evolution of all conservative variables. This removes short-wavelength noise that would otherwise interfere with clean convergence.

We compute the volume L_2 norm of the deviation of the conservative variables from their exact Bondi solutions:

$$\delta u = \left(\frac{\int |u - u_{\rm exact}|^2 \sqrt{\gamma} d^3x}{\int \sqrt{\gamma} d^3x} \right)^{1/2}. \tag{A36}$$

In Fig. 18 we plot the error norm measured by Eq. (A36) for all conservative variables after $100M$ of evolution for three different resolutions. These show that our results are converging at second-order, as expected (and as also observed in previous studies of this problem, e.g. [75,76]).

APPENDIX B: SPECTRAL METHOD FOR CYLINDERS AND SPHERES

When evolving the spacetime metric on a spectral grid, we try to adapt the domain decomposition to the geometry of the evolved fields. This often means using sections of a sphere, in the form of spherical shells or "cubed spheres." In black hole spacetimes, this is sufficient to cover the area surrounding the excised region within the apparent horizon. However, for neutron star spacetimes, a different approach is taken to cover the center of the star.

Polar and spherical coordinates are singular at the origin, creating difficulties if one tries to use tensor products of one-dimensional function bases. This same problem exists at the poles of a spherical surface. Spherical harmonics, $Y_l^m(\theta, \phi)$, provide a clean solution in that case, able to represent smooth functions without artificial boundaries and without severely restricting the time step allowed by the Courant-Friedrichs-Lewy stability limit [77]. For the radial "pole problem," Zernike polynomials and their higher dimensional generalizations provide a similar solution.

The use of Zernike polynomials in spectral methods over the unit disk was explored independently by Matsushima and Marcus [78] and by Verkley [79]. Notation varies throughout the literature, so we summarize ours here:

Denote an orthonormal azimuthal (Fourier) basis as

$$F_m(\phi) \equiv \begin{cases} \frac{1}{\sqrt{2\pi}} & m = 0 \\ \frac{1}{\sqrt{\pi}} e^{im\phi} & m > 0 \end{cases}. \tag{B1}$$

Then an arbitrary smooth function $f(\varpi, \phi)$ over the unit disk can be decomposed into its Fourier coefficients $f_m(\varpi)$:

$$f(\varpi, \phi) = \Re \sum_{m=0}^{m_{\rm max}} f_m(\varpi) F_m(\phi), \tag{B2}$$

where $m_{\rm max} = \lfloor N_\phi/2 \rfloor$, N_ϕ being the number of azimuthal collocation points. (Note that if N_ϕ is odd, the highest mode will lack a sine component.)

These Fourier coefficients can be further decomposed into a radial sub-basis $R_n^m(\varpi)$, composed of one-sided Jacobi polynomials multiplied by ϖ^m:

$$R_n^m(\varpi) \equiv \sqrt{2n+2}\, \varpi^m P^{(0,m)}_{(n-m)/2}(2\varpi^2 - 1), \tag{B3}$$

where $P_k^{(\alpha,\beta)}(x)$ represents the Jacobi polynomial of degree k. In this notation, the radial functions are only defined for $n \geq m$, $2|(n-m)$. For smooth functions, the $f_m(\varpi)$ satisfy the pole condition: $f_m(\varpi) \to \varpi^m$ as $\varpi \to 0$. This basis manifestly respects that condition.

The Zernike polynomials are then defined as

$$Z_m^n(\varpi, \phi) \equiv R_n^m(\varpi) F_m(\phi). \tag{B4}$$

They form an orthonormal basis for smooth functions over the unit disk:

$$f(\varpi,\phi)=\sum_{m=0}^{m_{\max}}\sum_{\substack{n=m\\ n+=2}}^{n_{\max}} f_{nm}Z_m^n(\varpi,\phi), \tag{B5}$$

where $n_{\max}=2N_\varpi-1$, N_ϖ being the number of radial collocation points. Note that if Gauss-Radau quadrature is used (placing collocation points on the outer boundary of the disk), then the highest-order radial basis functions should be normalized with respect to the quadrature rule (rather than analytically) or else omitted entirely. Specifications for the quadrature nodes and weights can be found in the references.

As mentioned by Livermore *et al.* [80], this can be generalized to filled spheres. In that case, a function $f(r,\theta,\phi)$ is decomposed into f_{nlm} such that

$$f(r,\theta,\phi)=\sum_{m=-m_{\max}}^{m_{\max}}\sum_{l=|m|}^{l_{\max}}\sum_{\substack{n=l\\ n+=2}}^{n_{\max}} f_{nlm}R_n^l(r)Y_l^m(\theta,\phi), \tag{B6}$$

where now $R_n^l(r)$ is given by

$$R_n^l(r)=\sqrt{2n+3}\,r^l P_{(n-l)/2}^{(0,l+1/2)}(2r^2-1), \tag{B7}$$

which corresponds to an integration weight of r^2 instead of ϖ. Here, $Y_l^m(\theta,\phi)$ are the spherical harmonics, and $l_{\max}=N_\theta-1$ for N_θ latitudinal collocation points.

Spectral methods can be susceptible to aliasing instabilities when, for instance, nonlinear interactions allow the creation of higher spectral modes through the mixing of lower ones. Appropriate filtering of the solution is therefore required for stable evolutions [81]. When using cylindrical and spherical domains in SpEC, we have found filtering to be unnecessary in the radial direction. Filtering in angular directions, meanwhile, is performed as for spherical shells [82].

APPENDIX C: MEASURING POWER IN AZIMUTHAL MODES

1. Preliminaries

Consider a function space spanned by a set of N basis functions $\phi_n(x)$ that are orthonormal with respect to a weight function $w(x)$. That is,

$$\int \phi_m(x)\phi_n(x)w(x)dx=\delta_{mn}. \tag{C1}$$

Further, assume the existence of a quadrature rule on a set of N collocation points x_i that is exact for all products of two functions in this space weighted by $w(x)$. In other words,

$$\sum_{i=0}^{N-1}\phi_m(x_i)\phi_n(x_i)w_i=\delta_{mn}, \tag{C2}$$

where w_i are the quadrature weights. Note that Gaussian quadrature meets this criterion for polynomial bases.

Let $f(x)$ be a member of this space, which we write as a linear combination of the basis functions:

$$f(x)=\sum_{n=0}^{N-1} f_n\phi_n(x), \tag{C3}$$

where the spectral coefficients f_n can be computed via

$$f_n=\int f(x)\phi_n(x)w(x)dx=\sum_{i=0}^{N-1} f(x_i)\phi_n(x_i)w_i. \tag{C4}$$

There exists a unique set of cardinal function $C_i(x)$ in this space with the property that

$$f(x)=\sum_{i=0}^{N-1} f(x_i)C_i(x), \tag{C5}$$

which we can solve for as follows: First, expand each $C_i(x)$ into its spectral coefficients $c_{n,i}$. Then we have

$$f(x)=\sum_{i=0}^{N-1} f(x_i)C_i(x)=\sum_{i=0}^{N-1} f(x_i)\sum_{n=0}^{N-1} c_{n,i}\phi_n(x),$$

which implies that

$$\sum_{n=0}^{N-1} f_n\phi_n(x)=\sum_{n=0}^{N-1}\left(\sum_{i=0}^{N-1} f(x_i)c_{n,i}\right)\phi_n(x),$$

and thus that

$$f_n=\sum_{i=0}^{N-1} f(x_i)\phi_n(x_i)w_i=\sum_{i=0}^{N-1} f(x_i)c_{n,i}.$$

This means that

$$c_{n,i}=\phi_n(x_i)w_i,$$

and therefore

$$C_i(x)=w_i\sum_{n=0}^{N-1}\phi_n(x_i)\phi_n(x). \tag{C6}$$

Observe that the cardinal functions obey the property

$$C_i(x_j)=\delta_{ij} \tag{C7}$$

and are orthogonal to one another with norm $\sqrt{w_i}$:

$$\int C_i(x)C_j(x)w(x)dx=w_i\delta_{ij}. \tag{C8}$$

Thus, the functions $\tilde{C}_i(x) \equiv C_i(x)/\sqrt{w_i}$ form another orthonormal basis for the space. [Note that this also provides a convenient way of computing the quadrature weights via $1/w_i = \sum_n \phi_n^2(x_i)$.]

2. Azimuthal power

Within the space of smooth functions defined in a cylindrical volume, consider the subspace spanned by a finite number of orthonormal basis functions of the form $P_l(z)Z_m^n(\varpi,\phi)$, where $P_l(z)$ is a basis for functions on a finite interval (such as Legendre polynomials) and $Z_m^n(\varpi,\phi) = R_n^m(\varpi)F_m(\phi)$ are the Zernike polynomials (see Appendix B for notation). Any function f in this subspace can be decomposed into spectral coefficients f_{lmn}. The amount of power in a given azimuthal mode m is defined to be

$$P_m[f] = \sum_l \sum_n |f_{lmn}|^2. \tag{C9}$$

One approach to computing this power for an arbitrary f is to compute each f_{lmn} by integrating $f(z,\phi,r)$ against the corresponding product of basis functions. If f is band-limited and the integration is of sufficiently high order, this will produce the exact result. Alternatively, f can be integrated against the set of cardinal functions along z and r. Here we show the equivalence of this nodal approach to the aforementioned modal one.

Let us denote our nodal power measurement by $Q_m[f]$:

$$Q_m[f] \equiv \sum_{i,j} \left| \iiint dz d\phi \varpi d\varpi f(z,\phi,\varpi) \tilde{C}_i(z) \tilde{C}_j^m(\varpi) F_m(\phi) \right|^2; \tag{C10}$$

here, $\tilde{C}_i(z)$ are the normalized cardinal functions associated with $P_l(z)$ and $\tilde{C}_j^m(\varpi)$ are the normalized cardinal functions associated with $R_n^m(\varpi)$. Expanding those cardinal functions in terms of their associated basis functions yields

$$\begin{aligned} Q_m[f] = \sum_{i,j} \Bigg| \iiint dz d\phi \varpi d\varpi f(z,\phi,\varpi) \\ \times \left(\sqrt{w_i^P} \sum\nolimits_l P_l(z_i) P_l(z) \right) \\ \times \left(\sqrt{w_j^R} \sum\nolimits_n R_n^m(\varpi_j) R_n^m(\varpi) \right) F_m(\phi) \Bigg|^2. \end{aligned} \tag{C11}$$

The presence of the weights suggests that the outer sums can be interpreted as integrals (note that the corresponding integrands are products of two basis functions and therefore exactly integrable by quadrature). And since the basis functions are orthonormal, the integral of a product of sums is equal to a sum of products. This simplifies the above expression to

$$Q_m[f] = \sum_{l,n} \left| \iiint dz d\phi \varpi d\varpi f(z,\phi,\varpi) P_l(z) R_n^m(\varpi) F_m(\phi) \right|^2. \tag{C12}$$

But the integral above is merely the projection of f onto the basis function indexed by l,m,n; thus

$$Q_m[f] = \sum_{l,n} |f_{lmn}|^2 = P_m[f]. \tag{C13}$$

This gives us two formally equivalent ways to measure the azimuthal power in f: one involving projections onto the modal basis, the other projecting onto the nodal (cardinal) basis. The latter matches an intuitive approach to avoiding the problem of power cancellation due to phase changes at different ϖ and z.

3. Error floor

Unfortunately, when performing these integrations on a finite volume domain, the Cartesian nature of the grid results in spurious power in $m = 4, 8, \ldots$ modes proportional to the error of the integration scheme (these "ambient grid modes" are also noted in studies where mode measurement is restricted to rings [14,19]). If the function does not approach zero at the boundary of the reference cylinder, then this spurious power will be significant because of the "Lego circle" approximation to the boundary.

This effect can be mitigated by windowing the data with a smooth function that transitions between one at the center and zero at the boundary. We have achieved good results using the window

$$W(\varpi) = \frac{1}{2}\{1 - \tanh[\tan(\pi(\varpi + 1/2))]\}. \tag{C14}$$

The effect of the windowing on the power spectrum can then be undone via a deconvolution (made robust by using a truncated singular value decomposition). Expressing the convolution of the spectrum as

$$C_{ij}\lambda_j = \lambda_i', \tag{C15}$$

the elements of $\boldsymbol{C}$ are given by

$$C_{ij} = \int W(\varpi) R_i^m(\varpi) R_j^m(\varpi) \varpi d\varpi. \tag{C16}$$

However, if the function being analyzed is entirely contained within the reference cylinder (by making its radius larger than that of the star, for instance), then this

windowing technique offers minimal improvement to the error floor. Additionally, for our setup, evolved data exhibits 100× more spurious power than initial data. The net result is that, at our resolution, $m = 4$ perturbations can only be measured if they are larger than 10^{-5} relative to the background. The act of windowing does make this procedure more robust, however, should the data expand beyond the chosen reference cylinder.

[1] S. Chandrasekhar, *The Silliman Foundation Lectures* (Yale University Press, New Haven, 1969).
[2] J. Toman, J. N. Imamura, B. K. Pickett, and R. H. Durisen, Astrophys. J. **497**, 370 (1998).
[3] M. Shibata, T. W. Baumgarte, and S. L. Shapiro, Astrophys. J. **542**, 453 (2000).
[4] M. Saijo, M. Shibata, T. W. Baumgarte, and S. L. Shapiro, Astrophys. J. **548**, 919 (2001).
[5] J. M. Centrella, K. C. B. New, L. L. Lowe, and J. D. Brown, Astrophys. J. **550**, L193 (2001).
[6] M. Shibata, S. Karino, and Y. Eriguchi, Mon. Not. R. Astron. Soc. **334**, L27 (2002).
[7] M. Shibata, S. Karino, and Y. Eriguchi, Mon. Not. R. Astron. Soc. **343**, 619 (2003).
[8] M. Saijo, T. W. Baumgarte, and S. L. Shapiro, Astrophys. J. **595**, 352 (2003).
[9] C. D. Ott, S. Ou, J. E. Tohline, and A. Burrows, Astrophys. J. Lett. **625**, L119 (2005).
[10] S. Ou and J. E. Tohline, Astrophys. J. **651**, 1068 (2006).
[11] M. Saijo and S. Yoshida, Mon. Not. R. Astron. Soc. **368**, 1429 (2006).
[12] P. Cerdá-Durán, V. Quilis, and J. A. Font, Comput. Phys. Commun. **177**, 288 (2007).
[13] C. D. Ott, H. Dimmelmeier, A. Marek, H.-T. Janka, I. Hawke, B. Zink, and E. Schnetter, Phys. Rev. Lett. **98**, 261101 (2007).
[14] S. Scheidegger, T. Fischer, S. C. Whitehouse, and M. Liebendörfer, Astron. Astrophys. **490**, 231 (2008).
[15] G. Corvino, L. Rezzolla, S. Bernuzzi, R. De Pietri, and B. Giacomazzo, Classical Quantum Gravity **27**, 114104 (2010).
[16] T. Kuroda and H. Umeda, Astrophys. J. Suppl. Ser. **191**, 439 (2010).
[17] A. L. Watts, N. Andersson, and D. I. Jones, Astrophys. J. Lett. **618**, L37 (2005).
[18] J. C. B. Papaloizou and J. E. Pringle, Mon. Not. R. Astron. Soc. **208**, 721 (1984).
[19] C. D. Ott, H. Dimmelmeier, A. Marek, H.-T. Janka, B. Zink, I. Hawke, and E. Schnetter, Classical Quantum Gravity **24**, S139 (2007).
[20] C. D. Ott, Classical Quantum Gravity **26**, 063001 (2009).
[21] K. D. Camarda, P. Anninos, P. C. Fragile, and J. A. Font, Astrophys. J. **707**, 1610 (2009).
[22] L. Franci, R. De Pietri, K. Dionysopoulou, and L. Rezzolla, Phys. Rev. D **88**, 104028 (2013).
[23] W. Fu and D. Lai, Mon. Not. R. Astron. Soc. **413**, 2207 (2011).
[24] M. Obergaulinger, P. Cerdá-Durán, E. Müller, and M. A. Aloy, Astron. Astrophys. **498**, 241 (2009).
[25] http://www.black-holes.org/SpEC.html.
[26] M. D. Duez, F. Foucart, L. E. Kidder, H. P. Pfeiffer, M. A. Scheel, and S. A. Teukolsky, Phys. Rev. D **78**, 104015 (2008).
[27] T. W. Baumgarte and S. L. Shapiro, *Numerical Relativity: Solving Einstein's Equations on the Computer* (Cambridge University Press, Cambridge, England, 2010).
[28] L. Baiotti, R. De Pietri, G. M. Manca, and L. Rezzolla, Phys. Rev. D **75**, 044023 (2007).
[29] F. Douchin and P. Haensel, Astron. Astrophys. **380**, 151 (2001).
[30] M. Shibata, K. Taniguchi, and K. Uryū, Phys. Rev. D **71**, 084021 (2005).
[31] G. B. Cook, S. L. Shapiro, and S. A. Teukolsky, Astrophys. J. **398**, 203 (1992).
[32] L. Lindblom, M. A. Scheel, L. E. Kidder, R. Owen, and O. Rinne, Classical Quantum Gravity **23**, S447 (2006).
[33] J. De Villiers and J. F. Hawley, Astrophys. J. **592**, 1060 (2003).
[34] J. C. McKinney and C. F. Gammie, Astrophys. J. **611**, 977 (2004).
[35] B. Giacomazzo, L. Rezzolla, and L. Baiotti, Phys. Rev. D **83**, 044014 (2011).
[36] D. M. Siegel, R. Ciolfi, and L. Rezzolla, Astrophys. J. Lett. **785**, L6 (2014).
[37] P. Mösta, S. Richers, C. D. Ott, R. Haas, A. L. Piro, K. Boydstun, E. Abdikamalov, C. Reisswig, and E. Schnetter, Astrophys. J. Lett. **785**, L29 (2014).
[38] E. N. Parker, Astrophys. J. **145**, 811 (1966).
[39] R. J. Tayler, Mon. Not. R. Astron. Soc. **161**, 365 (1973).
[40] D. J. Acheson and M. P. Gibbons, Phil. Trans. R. Soc. A **289**, 459 (1978).
[41] M. C. Begelman, Astrophys. J. **493**, 291 (1998).
[42] H. C. Spruit, Astron. Astrophys. **349**, 189 (1999).
[43] K. Kiuchi, S. Yoshida, and M. Shibata, Astron. Astrophys. **532**, A30 (2011).
[44] E. Pitts and R. J. Tayler, Mon. Not. R. Astron. Soc. **216**, 139 (1985).
[45] T. Foglizzo and M. Tagger, Astron. Astrophys. **287**, 297 (1994).
[46] S. A. Balbus and J. F. Hawley, Astrophys. J. **376**, 214 (1991).
[47] S. A. Balbus and J. F. Hawley, Astrophys. J. **400**, 610 (1992).
[48] S. A. Balbus and J. F. Hawley, Rev. Mod. Phys. **70**, 1 (1998).
[49] D. M. Siegel, R. Ciolfi, A. I. Harte, and L. Rezzolla, Phys. Rev. D **87**, 121302 (2013).
[50] P. J. Sutton, arXiv:1304.0210.

[51] O. Rinne, L. T. Buchman, M. A. Scheel, and H. P. Pfeiffer, Classical Quantum Gravity **26**, 075009 (2009).
[52] D. Shoemaker, LIGO Report No. LIGO-T0900288-v3, 2010.
[53] C. Loken, D. Gruner, L. Groer, R. Peltier, N. Bunn, M. Craig, T. Henriques, J. Dempsey, C.-H. Yu, J. Chen, L. J. Dursi, J. Chong, S. Northrup, J. Pinto, N. Knecht, and R. van Zon, J. Phys. Conf. Ser. **256**, 012026 (2010).
[54] F. Foucart, M. B. Deaton, M. D. Duez, L. E. Kidder, I. MacDonald, C. D. Ott, H. P. Pfeiffer, M. A. Scheel, B. Szilagyi, and S. A. Teukolsky, Phys. Rev. D **87**, 084006 (2013).
[55] M. Shibata and Y.-i. Sekiguchi, Phys. Rev. D **72**, 044014 (2005).
[56] K. S. Yee, IEEE Trans. Antennas Propag. **14**, 302 (1966).
[57] C. R. Evans and J. F. Hawley, Astrophys. J. **332**, 659 (1988).
[58] P. Londrillo and L. Del Zanna, J. Comput. Phys. **195**, 17 (2004).
[59] L. Del Zanna, O. Zanotti, N. Bucciantini, and P. Londrillo, Astron. Astrophys. **473**, 11 (2007).
[60] B. van Leer, J. Comput. Phys. **23**, 276 (1977).
[61] X.-D. Liu, S. Osher, and T. Chan, J. Comput. Phys. **115**, 200 (1994).
[62] G.-S. Jiang and C.-W. Shu, J. Comput. Phys. **126**, 202 (1996).
[63] Instead of adding a fixed $\epsilon = 10^{-6}$ to each smoothness indicator β, we instead add $\epsilon(1 + \sum_i y_i)$ with $\epsilon = 10^{-17}$.
[64] A. Harten, P. D. Lax, and B. van Leer, SIAM Rev. **25**, 35 (1983).
[65] S. C. Noble, C. F. Gammie, J. C. McKinney, and L. Del Zanna, Astrophys. J. **641**, 626 (2006).
[66] M. Galassi, J. Davies, J. Theiler, B. Gough, G. Jungman, P. Alken, M. Booth, and F. Rossi, *GNU Scientific Library Reference Manual*, 3rd ed. (Network Theory Limited, Bristol, United Kingdom, 2009).
[67] Z. B. Etienne, Y. T. Liu, V. Paschalidis, and S. L. Shapiro, Phys. Rev. D **85**, 064029 (2012).
[68] M. Boyle, L. Lindblom, H. P. Pfeiffer, M. A. Scheel, and L. E. Kidder, Phys. Rev. D **75**, 024006 (2007).
[69] M. D. Duez, Y. T. Liu, S. L. Shapiro, and B. C. Stephens, Phys. Rev. D **72**, 024028 (2005).
[70] S. S. Komissarov, Mon. Not. R. Astron. Soc. **303**, 343 (1999).
[71] A. Lichnerowicz, J. Math. Phys. (N.Y.) **17**, 2135 (1976).
[72] A. Majorana and A. M. Anile, Phys. Fluids **30**, 3045 (1987).
[73] C. F. Gammie, J. C. McKinney, and G. Tóth, Astrophys. J. **589**, 444 (2003).
[74] H. Kreiss and J. Oliger, *Methods for the Approximate Solution of Time Dependent Problems*, Global Atmospheric Research Programme (GARP): GARP Publication Series, Vol. 10 (GARP Publication, Geneva, 1973).
[75] B. Giacomazzo and L. Rezzolla, Classical Quantum Gravity **24**, S235 (2007).
[76] P. Mösta, B. C. Mundim, J. A. Faber, R. Haas, S. C. Noble, T. Bode, F. Löffler, C. D. Ott, C. Reisswig, and E. Schnetter, Classical Quantum Gravity **31**, 015005 (2014).
[77] R. Courant, K. Friedrichs, and H. Lewy, IBM J. Res. Dev. **11**, 215 (1967).
[78] T. Matsushima and P. S. Marcus, J. Comput. Phys. **120**, 365 (1995).
[79] W. T. M. Verkley, J. Comput. Phys. **136**, 100 (1997).
[80] P. W. Livermore, C. A. Jones, and S. J. Worland, J. Comput. Phys. **227**, 1209 (2007).
[81] B. Szilágyi, L. Lindblom, and M. A. Scheel, Phys. Rev. D **80**, 124010 (2009).
[82] L. E. Kidder, L. Lindblom, M. A. Scheel, L. T. Buchman, and H. P. Pfeiffer, Phys. Rev. D **71**, 064020 (2005).